

Recent progress of two-dimensional nanosheet membranes and composite membranes for separation applications

Wei Wang, Yanying Wei (✉), Jiang Fan, Jiahao Cai, Zong Lu, Li Ding, Haihui Wang (✉)

School of Chemistry & Chemical Engineering, South China University of Technology, Guangzhou 510640, China

© Higher Education Press 2021

Abstract Two-dimensional (2D) materials have emerged as a class of promising materials to prepare high-performance 2D membranes for various separation applications. The precise control of the interlayer nanochannel/sub-nanochannel between nanosheets or the pore size of nanosheets within 2D membranes enables 2D membranes to achieve promising molecular sieving performance. To date, many 2D membranes with high permeability and high selectivity have been reported, exhibiting high separation performance. This review presents the development, progress, and recent breakthrough of different types of 2D membranes, including membranes based on porous and non-porous 2D nanosheets for various separations. Separation mechanism of 2D membranes and their fabrication methods are also reviewed. Last but not the least, challenges and future directions of 2D membranes for wide utilization are discussed in brief.

Keywords membrane separation, 2D membranes, 2D materials, nanosheet

1 Introduction

In recent years, membrane-based separation technologies have received increasing attention attributing to lots of advantages such as the low energy consumption, easy operation, and environmental friendliness. Till now, polymeric membranes still dominate the membrane separation industry market because they are economic with good processibility, easy operation and competitive separation performance. However, for most polymeric membranes, there is a Robeson bound where an intrinsic

trade-off effect exists, i.e., highly permeable membranes generally with low selectivity and vice versa [1]. Membrane separation performance can be improved by reducing the thickness, where the ultimately achievable refinement in the thickness will be a one-atom-thick layer that can be achieved by two-dimensional (2D) materials. Hence, ultrathin 2D membranes have the possibility to achieve high permeability while retaining high selectivity by precisely tuning pore size, surpassing the upper bound of traditional membranes. The emergence of novel 2D materials, such as graphene, provides a new opportunity for membrane development. Discovery of monocrystalline graphitic films by Geim's group in 2004 has drawn widespread attention for 2D materials in some fields including the membrane separation [2]. Up till now, in addition to the earliest studied graphene, other 2D membranes have been prepared using building blocks of other materials such as zeolites, metal-organic frameworks (MOFs), covalent organic frameworks (COFs), graphene oxides (GOs), layered double hydroxides (LDHs), transition metal dichalcogenides (TMDs), MXenes and graphitic carbon nitrides (*g*-C₃N₄). Owing to the precise control of the interlayer nanochannel/sub-nanochannel or the pore size and reduction of mass transfer resistance, ultrathin membranes based on 2D nanosheets have become promising candidates for separation as the next-generation membrane, which could achieve high permeability while retaining high selectivity, surpassing the upper bound of traditional membranes.

2 Separation mechanism of 2D membranes

In the membrane separation process, ions or molecules pass through the membrane selectively where the membrane serves as the separation medium. In general, 2D membranes can be grouped into two types: porous nanosheets-based membranes and non-porous nanosheets-based membranes, usually named as stacking

Received July 15, 2020; accepted September 20, 2020

E-mails: ceyywei@scut.edu.cn (Wei Y);
hhwang@scut.edu.cn (Wang H)

2D lamellar membranes. The most conspicuous difference between these two types of 2D membranes is the separation mechanism and the mass transportation route.

Porous nanosheets-based membranes, such as 2D zeolite membranes, 2D MOF membranes, and 2D COF membranes, comprise nanosheets with intrinsic nano/subnanoporosity. For these porous nanosheets-based membranes, precise molecule sieving is primarily determined by the size of in-plane pores. Owing to the size of nanopores, porous nanosheets-based membranes only allow size-specific ions or molecules to pass through (Fig. 1(a)). According to the channel size and chemical environment, gas diffusion mechanisms of porous nanosheet membranes can be broadly divided into Knudsen diffusion, surface diffusion, molecular diffusion, and viscous flow [3]. The porous nanosheet membrane with regular nanopore structure and ultrathin thickness is a type of ideal separation membrane morphology, which could reduce mass transfer resistance and lead to ultrahigh permeance, while maintaining high selectivity resulting from the precise pore sieving. For example, Yang et al. successfully prepared several nanometer-thick $\text{Zn}_2(\text{bim})_4$ molecular sieve nanosheet membrane with an excellent H_2/CO_2 separation factor of 291 accompanied by an H_2 permeance of 2700 gas permeation unit (GPU), far surpassing the Robeson upper bound [4].

Stacking 2D lamellar membranes, such as 2D GO, LDH, MXene and TMD membranes, comprises nanosheets without inherent in-plane pores. The ions or molecules transportation and sieving are achieved by the controlled interlayer nanochannels/subnanochannels formed by stacked nanosheets. As shown in Fig. 1(b), the interlayer

spacing between the neighboring nanosheets allows transport of small ions or molecules while blocks large ions or molecules. For the 2D lamellar membranes, design and tuning the interlayer spacing are important for membrane separation performance, and significant achievements have been made in this field [5–7].

In general, there are two types of pathway for mass transportation in 2D membranes, including the inter-sheet pathway A, (referring to interlayer spacing between nanosheets) and the inner-sheet pathway B, (referring to in-plane pore-based transport pathway). For gas separation, the membrane permeability was calculated by the following equation [8]:

$$P = \left(\frac{1}{h}\right) \left[\left(\frac{\varepsilon_A}{\tau_A}\right) D_A K_A + \left(\frac{\varepsilon_B}{\tau_B}\right) D_B K_B \right],$$

where h is the membrane thickness; ε and τ are the porosity and tortuosity for pores of pathways A and B, respectively; D and K are the gas diffusivity and adsorption equilibrium constant in pathways A or B, respectively. In particular, the tortuosity (τ) of 2D membranes can be approximately calculated as the ratio of the lateral size to thickness of nanosheets, while the porosity (ε) is related to the interlayer d -spacing, the thickness, and porosity of nanosheets.

For inter-sheet pathway A, the diffusion length can be estimated by the Nielsen transport model [9]:

$$l = h + N \frac{L}{2},$$

$$N = \frac{h}{d + W},$$

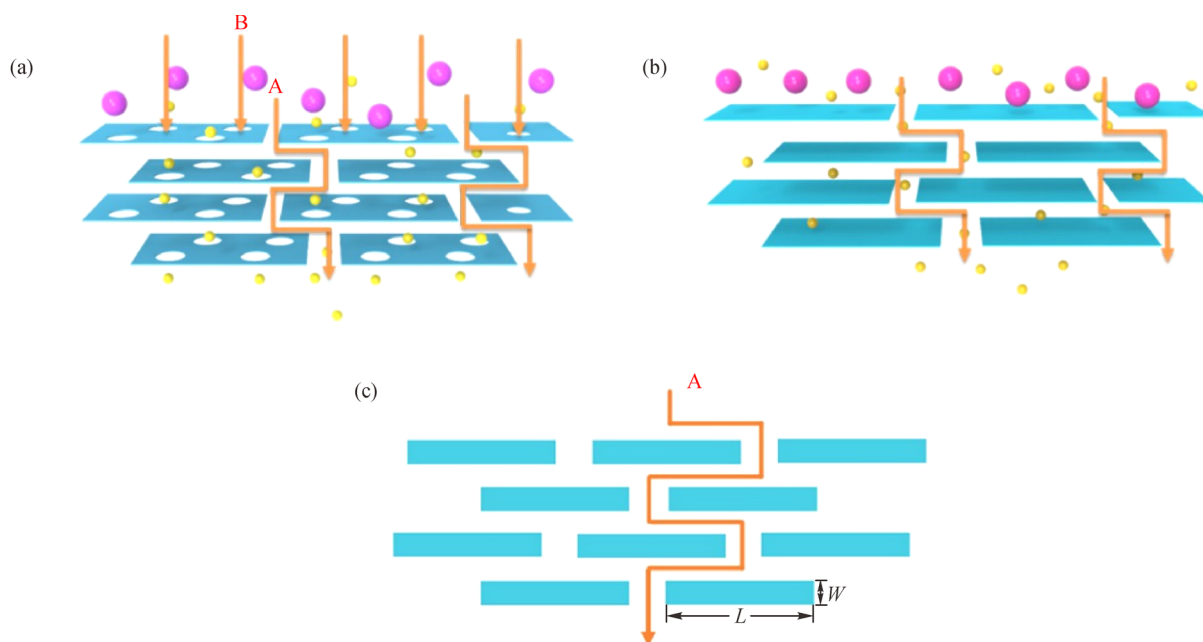


Fig. 1 (a) Transport model of porous nanosheets-based membranes; (b) transport model of 2D lamellar membranes; (c) transport model of inter-sheet pathway A.

where l is the diffusion length, h is the membrane thickness, L and W are the lateral dimensions and thickness of the platelet, respectively, and d is the effective distance between the platelets.

3 Preparation of 2D nanosheets and 2D membranes

A high-performance 2D membrane needs high-quality 2D nanosheets and the precise assembly of nanosheets. Hence, preparation strategies of 2D nanosheets and 2D membranes are essential issues to realize the membrane separation. Many synthetic methods to prepare 2D nanosheets have been developed, such as mechanical exfoliation, intercalation exfoliation, chemical vapor deposition, and wet-chemical syntheses. In general, there are two types of strategies to synthesize 2D nanosheets, i.e., the top-down route and the bottom-up route. The former refers to the disintegration of bulky materials into delaminated nanosheets and the latter refers to direct synthesis from the corresponding starting materials. Several reviews on the preparation of various 2D materials have compared the advantages and disadvantages of different methods to prepare 2D nanosheets [10–12].

Pressure-assisted filtration is the most widely used method to fabricate 2D membranes, which has distinct advantages over other methods due to its simple operation and low cost. Layer-by-layer assembly is the process of depositing multilayers with some interactions such as electrostatic interactions, hydrogen bonds and covalent interactions. Although high requirement for equipment, high-quality monolayer membranes can be obtained through layer-by-layer process. The deposition of nanosheets are achieved by vertically lifting the substrate in the LangmuirBlodgett process while the substrate was contacted face-to-face with the nanosheet layer at the interface in the LangmuirSchäfer process. In recent years, electrostatic deposition has been widely concerned on the fabrication of 2D membranes, although electrostatic deposition is only suitable for the assembly of charged 2D materials. Synthesis of 2D nanosheets and preparation methods for 2D membranes are also discussed.

4 Different types of 2D membranes

As discussed above, 2D membranes can be assembled by two types of nanosheets. One is non-porous 2D nanosheets, such as GOs [13–15], MXenes [16,17], TMDs [18,19]. In the 2D membranes constructed by non-porous nanosheets, the mass can be transferred through the interlayer spacing between nanosheets. The other type is porous 2D nanosheets such as zeolites [20,21], MOFs [4,22,23], COFs [24,25] and $g\text{-C}_3\text{N}_4$ [26,27]. In this section, the development progress and

recent breakthrough of different types of 2D membranes are introduced to show high potentials for membrane separations.

4.1 2D membranes based on porous nanosheets

4.1.1 Zeolite membranes

Zeolites are microporous materials based on crystalline silica with the pore size in the range of 0.25 nm to more than 1 nm [28]. In 2009, Ryoo's group achieved the single-unit-cell thick Mobil Five (MFI) nanosheets through the zeolite-SDA-functionalized surfactant [29,30]. As a new class of zeolite nanosheets, have received more and more attentions in terms of its property and application in membrane separation. In 2011, Tsapatsis's group successfully prepared MFI-nanosheet membranes via simple filtration. Owing to non-selective gaps between the neighboring MFI nanosheets, these films did not show any separation performance for *p*-xylene and *o*-xylene [31]. To address this problem, they prepared 200 nm-thick MFI-nanosheet membranes via secondary growth approach on filtered oriented MFI nanosheet layers containing non-selective gaps, exhibiting promising molecular sieving property for *p*-xylene and *o*-xylene [32]. In 2013, Yoon's group reported a new method of membrane growth named as "gel-free secondary growth" and obtained 200-nm-thick silicalite-1 membrane, exhibiting a good *p*-xylene/*o*-xylene separation factor of 1050 accompanied by a *p*-xylene permeance of $13 \times 10^{-8} \text{ mol}\cdot\text{m}^{-2}\cdot\text{s}^{-1}\cdot\text{Pa}^{-1}$ [33]. Then, Tsapatsis's and Yoon's groups changed the seeding procedure to avoid scale-up challenges arising because of manually rubbing the seed crystals on the support. They combined filter-coating seeding method and gel-less secondary growth to prepare oriented MFI membranes as thin as 100 nm. Compared to the silicalite-1 membrane (200 nm) reported by Yoon's group, the obtained thinner membrane (100 nm) showed enhanced *p*-xylene permeance ($2.4 \times 10^{-7} \text{ mol}\cdot\text{m}^{-2}\cdot\text{s}^{-1}\cdot\text{Pa}^{-1}$) but a reduced separation factor for *p*-xylene/*o*-xylene (500) [34].

In general, top-down and bottom-up are two types of strategies to synthesize 2D nanosheets. The above-mentioned method for the synthesis of MFI nanosheets belongs to top-down strategy, which is hard for the preparation of high-aspect-ratio nanosheets. In 2017, Tsapatsis's group made a breakthrough in the synthesis strategy of zeolite nanosheets. They successfully synthesized the high-aspect-ratio MFI nanosheets, which were used to prepare a membrane via a gel-free secondary growth. Compared to membranes made from exfoliated nanosheets, the obtained membrane possessed a high *p*-xylene permeance of $0.56 \times 10^{-6} \text{ mol}\cdot\text{m}^{-2}\cdot\text{s}^{-1}\cdot\text{Pa}^{-1}$, with a *p*-xylene/*o*-xylene separation factor of 2000 [35]. Then, Tsapatsis's group applied a novel floating particle

coating strategy to prepare MFI nanosheet seed layers on directly synthesized MFI nanosheets (Fig. 2(a)). Compared to the Langmuir-Schäfer strategy, the floating particle coating strategy can produce higher-density zeolite nanosheet seed coatings on porous supports (Fig. 2(b)), resulting in MFI membrane with an excellent selectivity of *p*-xylene/*o*-xylene over 10000 and a maximum *p*-xylene permeance of $2.9 \times 10^{-7} \text{ mol} \cdot \text{m}^{-2} \cdot \text{s}^{-1} \cdot \text{Pa}^{-1}$ via a gel-free secondary growth of the MFI nanosheet coating [20]. Furthermore, Cao et al. prepared the ZSM-5 zeolite nanosheets with very large aspect ratios and nanometer-scale thickness by the bottom up method and then prepared a 2D ZSM-5 membrane by dip coating followed with consolidation by the vapor-phase crystallization on a porous α -Al₂O₃ support (Fig. 2(c)). The obtained membrane showed a high salt rejection rate (> 99.8%) with a water flux of $3.69 \text{ L} \cdot \text{m}^{-2} \cdot \text{h}^{-1}$ for the pervaporation desalination of 24 wt% NaCl solution [21]. Recently, Min et al. made a progress on the preparation of 2D MFI membranes on α -alumina hollow fiber supports for large-scale molecular sieving applications via vacuum filtration and two sequential hydrothermal treatments. The obtained membrane exhibited a separation factor of 58 for *n*-butane/*i*-butane accompanied by a *n*-butane permeance of 1923 GPU [36].

In addition to 2D MFI zeolite membranes, other 2D zeolite nanosheets such as MCM-22 [37,38], AMH-3 [39,40], and JDF-L1 [41–43] were also assembled into membranes for separation applications. Recently, Wei et al. designed a sodalite zeolite membrane via the hydrothermal crystallization of sodalite zeolite on a α -Al₂O₃ support with the predeposition of MCM-22 flakes. The obtained sodalite zeolite membrane demonstrated a permeation flux of $4.4 \text{ kg} \cdot \text{m}^{-2} \cdot \text{h}^{-1}$ accompanied by a good pervaporation separation of water/ethanol (> 10000) [44]. Besides the preparation of pure 2D zeolite membranes, 2D zeolite nanosheets could be applied to nanocomposite membranes to solve trade-off effect [39–43,45]. For example, Galve et al. prepared a new type of mixed matrix membranes (MMMs) by combining two types of porous fillers (MCM-41 and JDF-L1). The obtained membrane demonstrated an H₂/CH₄ selectivity of 32 accompanied by an H₂ permeability of 440 Barrer [43].

4.1.2 MOF membranes

MOF nanosheets, as an important group of 2D materials, are promising candidates for membrane separation. 2D MOF membranes have drawn widespread attention for separation attributing to their advantages such as ultrathin thickness, high specific area, and tunable molecular structures. Recently, Peng and Yang summarized a series of research studies about the MOF nanosheet-based membranes for separation [46]. Traditional MOF materials used for membranes mainly possess 3D framework; however, in 2014, Peng et al. made a great breakthrough

in the field of 2D MOF membranes. The challenge in preparing high-performance 2D-MOF membranes with exfoliated MOF nanosheets from layered MOFs is retaining the morphological and structural integrity of MOF nanosheets. To address such issue, they successfully prepared Zn₂(bim)₄ nanosheets with a thickness of 1.12 nm and lateral dimension of 1.5 mm by low speed wet ball-milling and ultrasonic exfoliation. Another challenge is in preparing high-performance ultrathin 2D-MOF membranes without defects. They used a hot-drop coating method, where the dispersed Zn₂(bim)₄ nanosheets were assembled on a heated porous α -Al₂O₃ support (Fig. 3(a)). The resulting ultrathin membrane possessed a good H₂/CO₂ separation factor of 291, but an H₂ permeance of 2700 GPU [4]. The H₂ permeance of this resulting membrane is higher than other membranes for H₂/CO₂ separation and the H₂/CO₂ separation factor of this membrane is also quite high. Then, Peng et al. adopted similar method to prepare sub-10 nm-thick Zn₂(bim)₃ membranes, displaying an H₂/CO₂ separation factor of 166 accompanied by an H₂ permeance of $8 \times 10^{-7} \text{ mol} \cdot \text{m}^{-2} \cdot \text{s}^{-1} \cdot \text{Pa}^{-1}$ [22]. In 2017, Wang et al. reported the freeze-thaw method to fabricate MAMS-1 nanosheets, where the MAMS-1 crystals were freeze-dried in liquid nitrogen bath followed by treatment using hot water to thaw. MAMS-1 crystals were exfoliated into layered nanosheets by the shear force produced in repeated freeze-thaw cycles. In addition, they used a hot-drop coating to fabricate MAMS-1 membranes. The obtained 40-nm membrane exhibited an H₂/CO₂ selectivity of 235 ± 14 accompanied by an H₂ permeance of 553 ± 228 GPU [23]. Very recently, Zhang's group successfully prepared exfoliated water-stable Al-MOF nanosheets. The ultrathin Al-MOF membrane formed by vacuum filtration showed a high water flux of $2.22 \text{ mol} \cdot \text{m}^{-2} \cdot \text{h}^{-1} \cdot \text{bar}^{-1}$ and rejection rates of nearly 100% for inorganic ions, better than the most reported 2D laminar membranes on the water/ion selectivity (Fig. 3(b)), making 2D MOF membranes as promising candidates for ion separation [47].

Besides the top-down method, Rodenas et al. successfully prepared highly crystalline and intact CuBDC nanosheets via a bottom-up synthesis strategy in 2015. Furthermore, these CuBDC nanosheets were used as fillers to prepare CuBDC/polyimide (PI) MMMs. The resulting ns-CuBDC/PI membrane exhibited a higher CO₂/CH₄ selectivity (88.2 ± 1.3) than the polymeric membrane and the *b*-CuBDC/PI membrane [48]. Inspired by their work, many reports about MOF nanosheet-based MMMs have caught public attention [49–51]. Yang et al. used GO to repair the defects between the junctions of CuBDC nanosheets, and the obtained CuBDC-GO composite membranes showed an H₂ permeance of $9.6 \times 10^{-7} \text{ mol} \cdot \text{m}^{-2} \cdot \text{s}^{-1} \cdot \text{Pa}^{-1}$ with an H₂/CO₂ separation selectivity of 95.1 [52]. Zhong et al. prepared two types of 2D ZIF-L membranes with different orientations (*b*-oriented and *c*-oriented) and demonstrated the important effect of

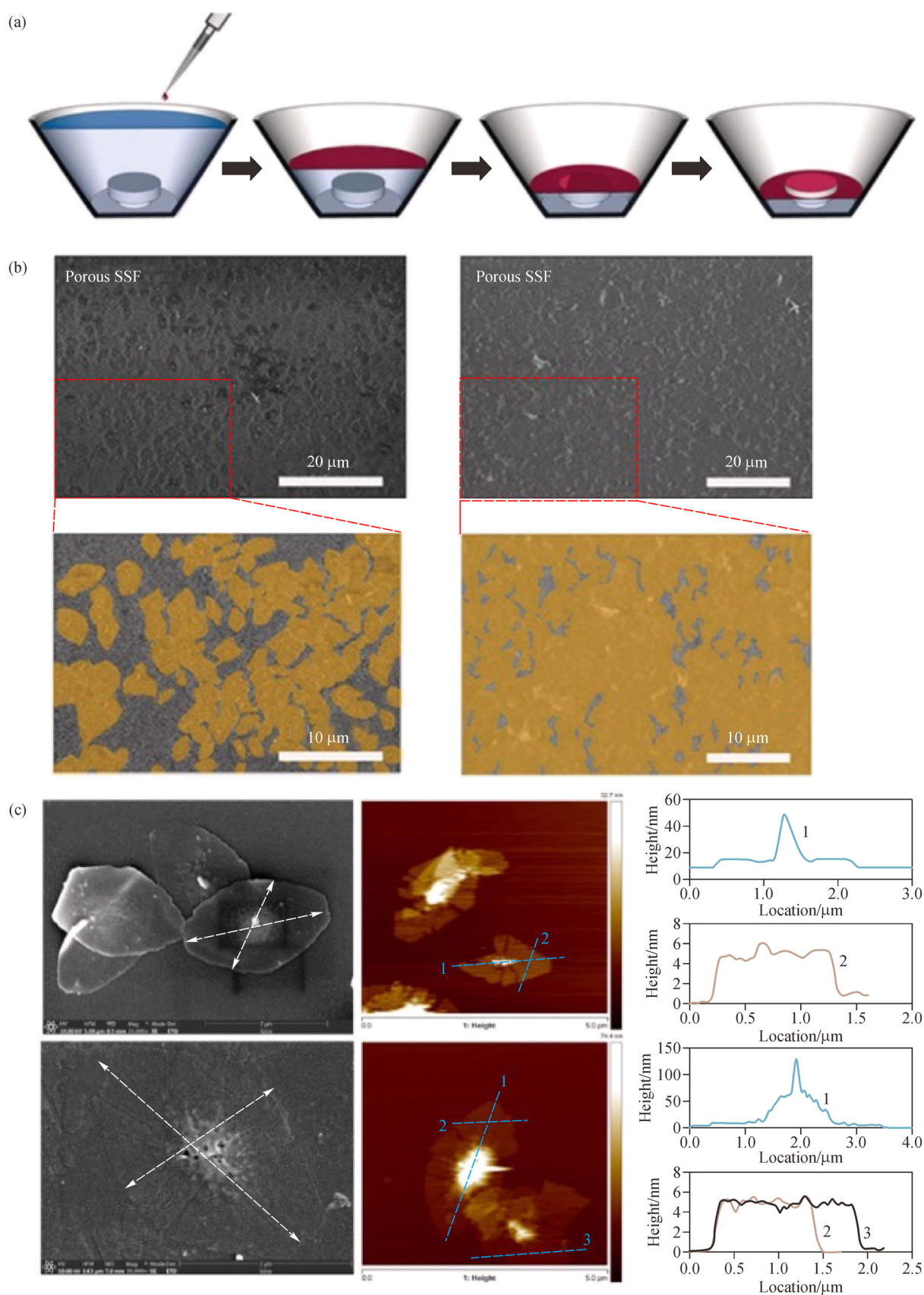


Fig. 2 (a) Illustration of the floating-particle coating method to prepare MFI nanosheet monolayer seed coating; (b) SEM images of MFI nanosheet seed coatings on porous substrate via the Langmuir-Schäfer (left) and the floating-particle coating (right). Reprinted with permission from Ref. [20], copyright 2018 Wiley VCH; (c) Microscopic characterizations of the silicalite nanosheets. Reprinted with permission from Ref. [21], copyright 2018 American Association for the Advancement of Science.

controlling crystal orientation on the ZIF membrane separation performance. The *b*-oriented and *c*-oriented ZIF-L membranes were both prepared by the secondary growth method. However, the seeding procedures were different. The *b*-oriented ZIF-L membrane had a secondary growth from a randomly oriented seed layer by dip-coating while the *c*-oriented ZIF-L membrane was prepared by secondary growth from a *c*-oriented ZIF-L crystal layer by vacuum filtration with polyethyleneimine (Fig. 3(c)). Owing to different paths of the molecule transport, the obtained *c*-oriented ZIF-L membrane with a smaller pore had a positive effect on the gas separation [53]. In order to improve separation performance, 2D Zn-TCP(Fe) nanosheets, obtained from a direct synthesis, were cross-linked by polycations followed by a simple vacuum filtration to prepare 2D MOF membranes. The obtained 2D Zn-TCP(Fe) membrane exhibited an excellent water permeance of $4243 \text{ L} \cdot \text{m}^{-2} \cdot \text{h}^{-1} \cdot \text{bar}^{-1}$ accompanied by a rejection rate of 98.2% for methyl red [54].

In addition to the preparation of 2D MOF membranes on

porous flat or disc-shaped substrates, Zhang's group prepared the 2D ZIF membranes on porous tubes for possible industrial applications. They reported the formation of $\text{Zn}_2(\text{bim})_4$ nanosheet tubular membranes via ZnO self-conversion growth in a GO confined space, and the obtained oriented membrane exhibited an H_2 permeance of $1.4 \times 10^{-7} \text{ mol} \cdot \text{m}^{-2} \cdot \text{s}^{-1} \cdot \text{Pa}^{-1}$ accompanied by a selectivity of 106 for H_2/CO_2 (Fig. 4(a)) [55]. Then, they advanced the preparation of 2D ZIF membranes on porous alumina tubes via ZnO self-conversion with ammonia assistance. The obtained 50-nm-thick $\text{Zn}_2(\text{bim})_4$ nanosheet membrane exhibited an H_2 permeance of $2.04 \times 10^{-7} \text{ mol} \cdot \text{m}^{-2} \cdot \text{s}^{-1} \cdot \text{Pa}^{-1}$ accompanied by selectivities of 53, 67, and 90 for H_2/CO_2 , H_2/N_2 and H_2/CH_4 , respectively [56]. More recently, the same group achieved the direct growth of the 57-nm-thick $\text{Co}_2(\text{bim})_4$ nanosheet tubular membrane with an H_2 permeance of $17.2 \times 10^{-8} \text{ mol} \cdot \text{m}^{-2} \cdot \text{s}^{-1} \cdot \text{Pa}^{-1}$ accompanied by a selectivity of 58.7 for H_2/CO_2 via ligand vapor phase transformation of the Co-based gel layer (Fig. 4(b)) [57].

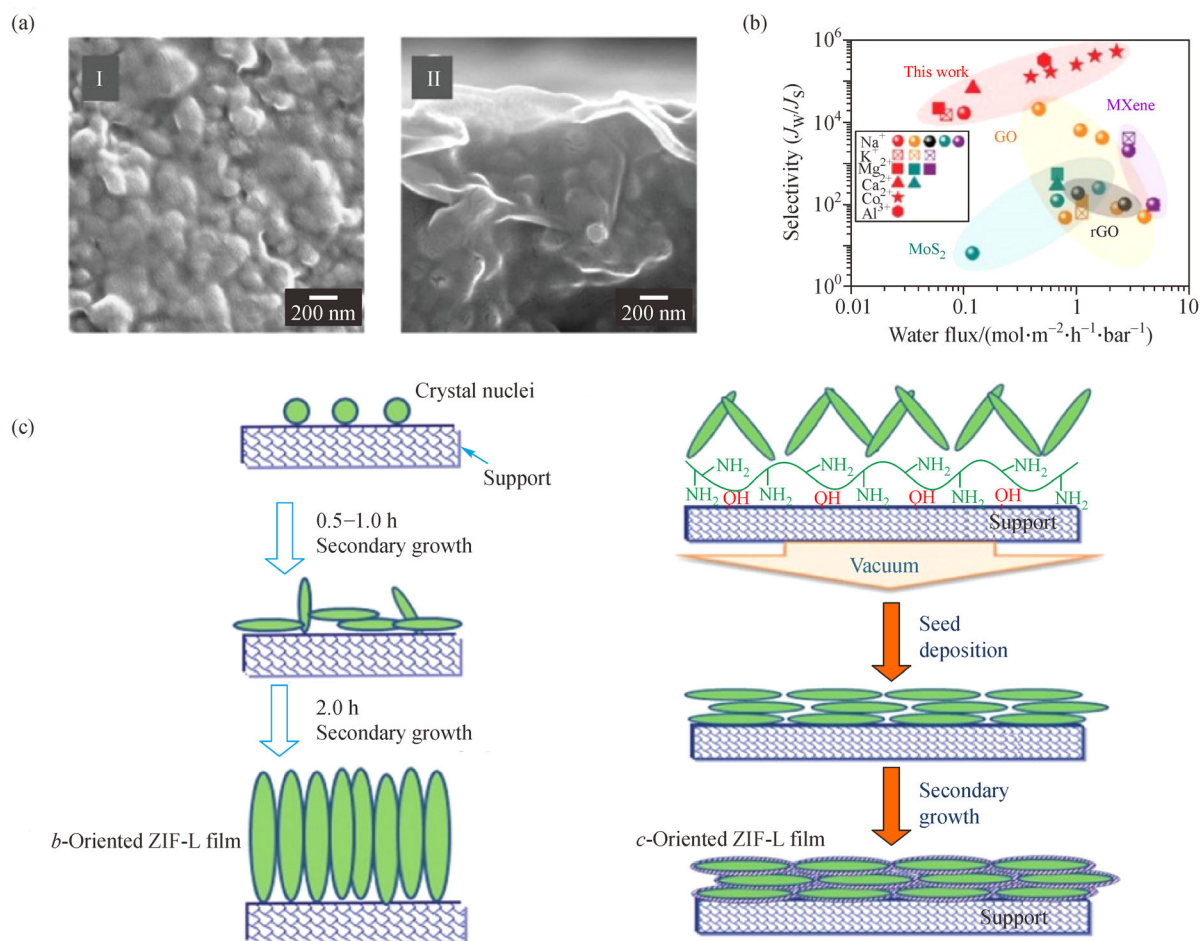


Fig. 3 (a) SEM images of (I) the top view and (II) cross-section view of an ultrathin $\text{Zn}_2(\text{bim})_4$ nanosheet on $\alpha\text{-Al}_2\text{O}_3$ support. Reprinted with permission from Ref. [4], copyright 2014 American Association for the Advancement of Science; (b) Comparison of the Al-MOF membrane for ion separation with other representative 2D lamellar membranes. Reprinted with permission from Ref. [47], copyright 2020 American Association for the Advancement of Science; (c) Illustration of the fabrication of *b*-oriented ZIF-L film and *c*-oriented ZIF-L film. Reprinted with permission from Ref. [53], copyright 2015 The Royal Society of Chemistry.

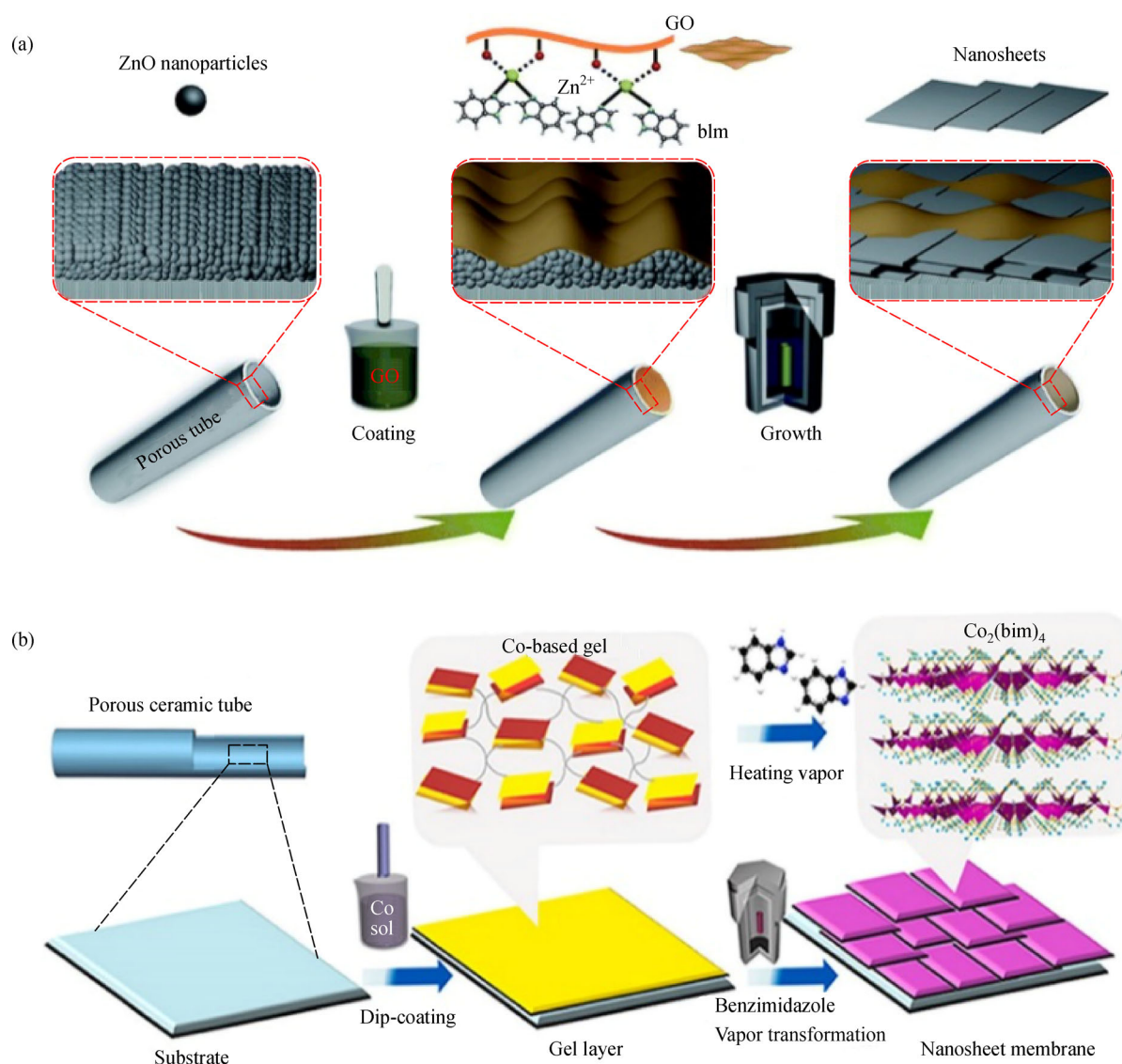


Fig. 4 (a) Illustration of $Zn_2(bim)_4$ nanosheet membranes formation via GO guided self-conversion of ZnO nanoparticles. Reprinted with permission from Ref. [55], copyright 2018 The Royal Society of Chemistry. (b) Illustration of $Co_2(bim)_4$ nanosheet membranes formation via vapor phase transformation of Co-based gel. Reprinted with permission from Ref. [57], copyright 2018 Elsevier.

4.1.3 COF membranes

In recent years, COF nanosheets have also been assembled for membranes. Many simulation results have proved that 2D COF is a type of promising material for membrane separation [58–60]. Interfacial synthesis and exfoliation methods are classical methods for the fabrication of high-performance 2D COF membranes. Recently, Yao et al. prepared ultrathin Tp-AD, Tp-Pa and Tp-BD nanosheets with a large area via azobenzene-assisted exfoliation method. The obtained Tp-AD membrane displayed a water flux of $596 \text{ L} \cdot \text{m}^{-2} \cdot \text{h}^{-1} \cdot \text{bar}^{-1}$ and a RB rejection rate up to 98% [61]. In addition to the widely used exfoliation method, Dey et al. prepared COF membranes by an

interfacial crystallization method, and the resulting Tp-Bpy film demonstrated a high solute rejection with an acetonitrile permeance of $339 \text{ L} \cdot \text{m}^{-2} \cdot \text{h}^{-1} \cdot \text{bar}^{-1}$ [62]. Matsumoto et al. reported the formation of free-standing TAPB-PDA COFs films with a high rejection (up to 91%) of R-WT via interfacial polymerization catalyzed by Lewis acid [63]. Besides, Fan et al. reported tubular imine-linked COF-LZU1 membranes via *in situ* solvothermal growth. The resulting membrane possessed an outstanding water stability and a good water permeance about $760 \text{ L} \cdot \text{m}^{-2} \cdot \text{h}^{-1} \cdot \text{MPa}^{-1}$ with a rejection rate of 98% for chrome black T [64].

At present, 2D COF membranes are limited in the separation of small molecules. One of the main problems is

the relatively larger pore size of 2D COFs membranes than the size of most gas molecules. Hence, applications of 2D COF membranes for separation of small molecules are still a great challenge. Discussions regarding the control of the pore sizes of 2D COF membranes have dominated research in recent years [24,25,65,66]. Caro's group designed a COF-COF bilayer membrane via a temperature-swing solvothermal approach. Owing to the formation of interlaced pore networks, the obtained COF-LZU1-ACOF-1 bilayer membrane with more appropriate pore size showed higher separation selectivity for H_2/CO_2 , H_2/N_2 and H_2/CH_4 than the individual COF-LZU1 and ACOF-1 membranes [65]. Yang et al. reported a series of COF membranes assembled by 2D COF nanosheets and 1D cellulose nanofibers (CNFs) (Fig. 5(a)). The pore size of the 2D COF membrane reduced with the sheltering

function of CNFs, endowing the resulting membrane with accurate molecular sieving ability to meet different separation demands [24]. More recently, Li et al. reduced the pore size to sub-nm scale (~ 0.6 nm) via adjusting the stacking mode of COF layers from AA to AB stacking, and the resulting AB stacking COF membranes with smaller pore showed high potentials in membrane separation (Fig. 5(b)). The idea in their study can also be applied to design other 2D membranes with suitable pore size for the accurate molecular sieving [66]. Recently, Ying et al. designed a 2D COF membrane using anionic TpPa-SO₃Na and cationic TpEBr nanosheets with different pore sizes via layer-by-layer assembly. Compared to the COF-COF bilayer membrane (ca. 1 μ m) reported by Caro's group, the obtained ultrathin hybrid TpEBr@TpPa-SO₃Na membrane (41 nm) with small pore and compact dense nanosheet

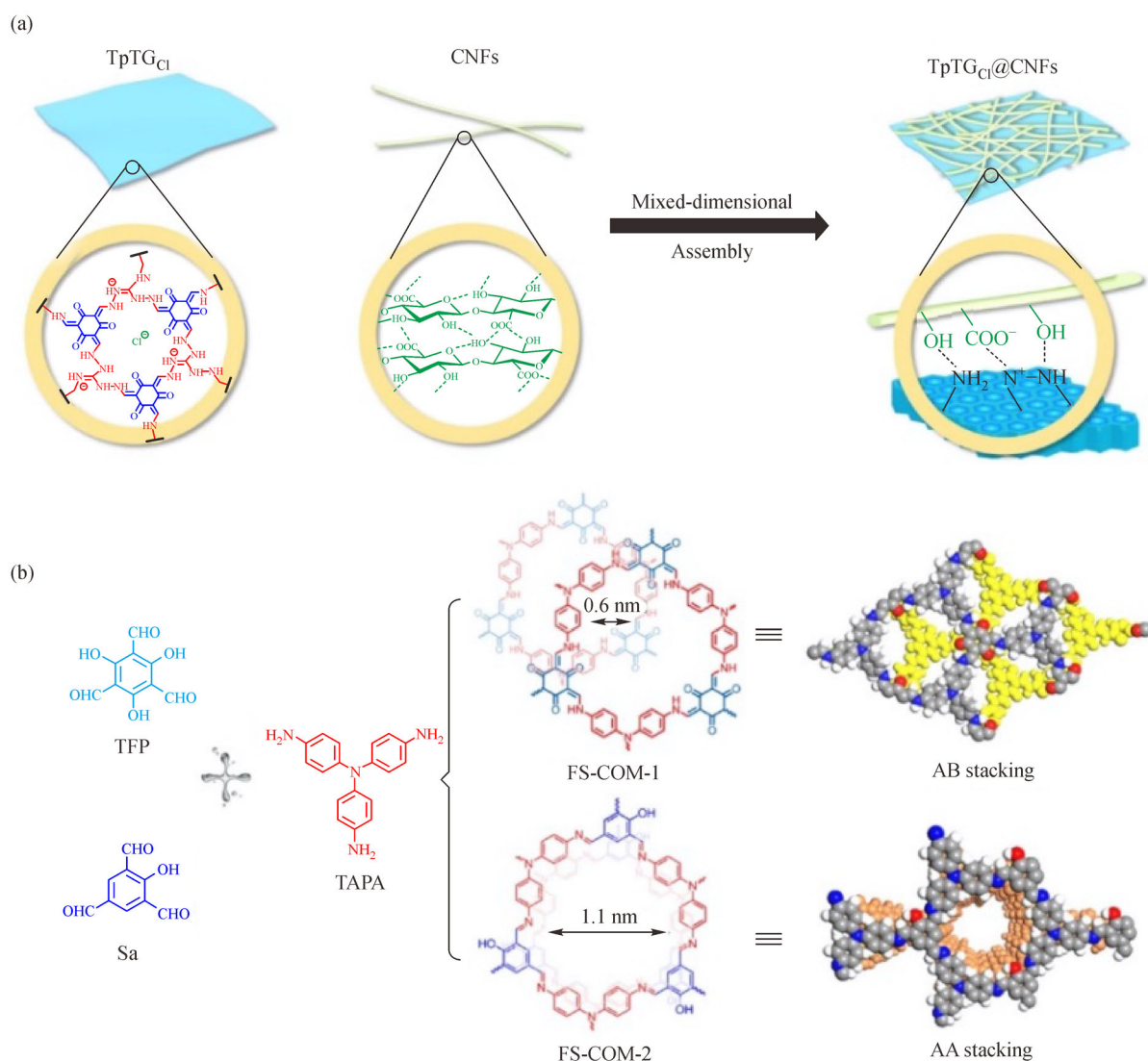


Fig. 5 (a) Illustration of CNFs/COF membrane formation. Reprinted with permission from Ref. [24], copyright 2019 Nature Publishing Group; (b) Structures of the AB stacking and the AA stacking COF membrane. Reprinted with permission from Ref. [66], copyright 2020 Nature Publishing Group.

membrane structure displayed a higher H_2 permeance of 2566 GPU accompanied by a selectivity of 22.6 for H_2/CO_2 [25].

4.1.4 Graphitic carbon nitride membranes

Because of the ordered triangular 0.311 nm-sized nanopores, $g-C_3N_4$ have received more and more attentions for membrane separation. Many molecular simulations provide a bright prospect of $g-C_3N_4$ membranes in separation [67,68]. In 2017, our group prepared the 2D $g-C_3N_4$ membranes with artificial nanopores and self-supporting spacers (Fig. 6). The obtained 160 nm-thick $g-C_3N_4$ membrane displayed a water flux of $29 L \cdot m^{-2} \cdot h^{-1} \cdot bar^{-1}$ and a rejection rate of 87% for Evans blue [26]. To enhance the water permeance of $g-C_3N_4$ membranes further, our group prepared polyacrylic acid-modified $g-C_3N_4$ nanosheet membranes with the polyacrylic acid tuning nanochannels. Owing to a slight increase in interlayer spacing, the obtained $g-C_3N_4$ -PAA hybrid membrane demonstrated a higher water flux of $117 L \cdot m^{-2} \cdot h^{-1} \cdot bar^{-1}$ accompanied by a similar rejection rate of 83% for Evans blue [69]. Recently, in order to improve the separation performance of the pure $g-C_3N_4$ membrane, Ran et al.

enlarged the interlayer spacing of $g-C_3N_4$ adjacent nanosheets by embedding molecules containing SO_3H . They successfully prepared the SPPO/ $g-C_3N_4$ membranes, exhibiting a superior selective rejection of 100% to methyl blue and with a high water permeability of $8867 L \cdot m^{-2} \cdot h^{-1} \cdot bar^{-1}$ [27]. Besides, Wang et al. designed $g-C_3N_4$ based membranes by incorporating sulfate anion or camphorsulfonic acid anion into protonated layers. The obtained membrane showed highly enantioselective permeation, endowing graphite phase carbon nitride as a promising material for chiral membrane [70]. Moreover, several reviews about $g-C_3N_4$ -based MMMs have emerged [71–77]. For instance, Gao et al. prepared acidified $g-C_3N_4$ -PA MMMs by incorporating acidified $g-C_3N_4$ into a polyamide selective layer by interfacial polymerization, and the as-obtained $g-C_3N_4$ -PA MMMs exhibited a higher water flux ($45 L \cdot m^{-2} \cdot h^{-1}$) than the pure PA membranes with an NaCl rejection of 98.6% [76].

4.1.5 Nanoporous graphene (NPG) membranes

Graphene, as a well-known 2D material, was first exfoliated from graphite by Geim and Novosolov in 2004 [2]. The defect-free single-layer graphene is

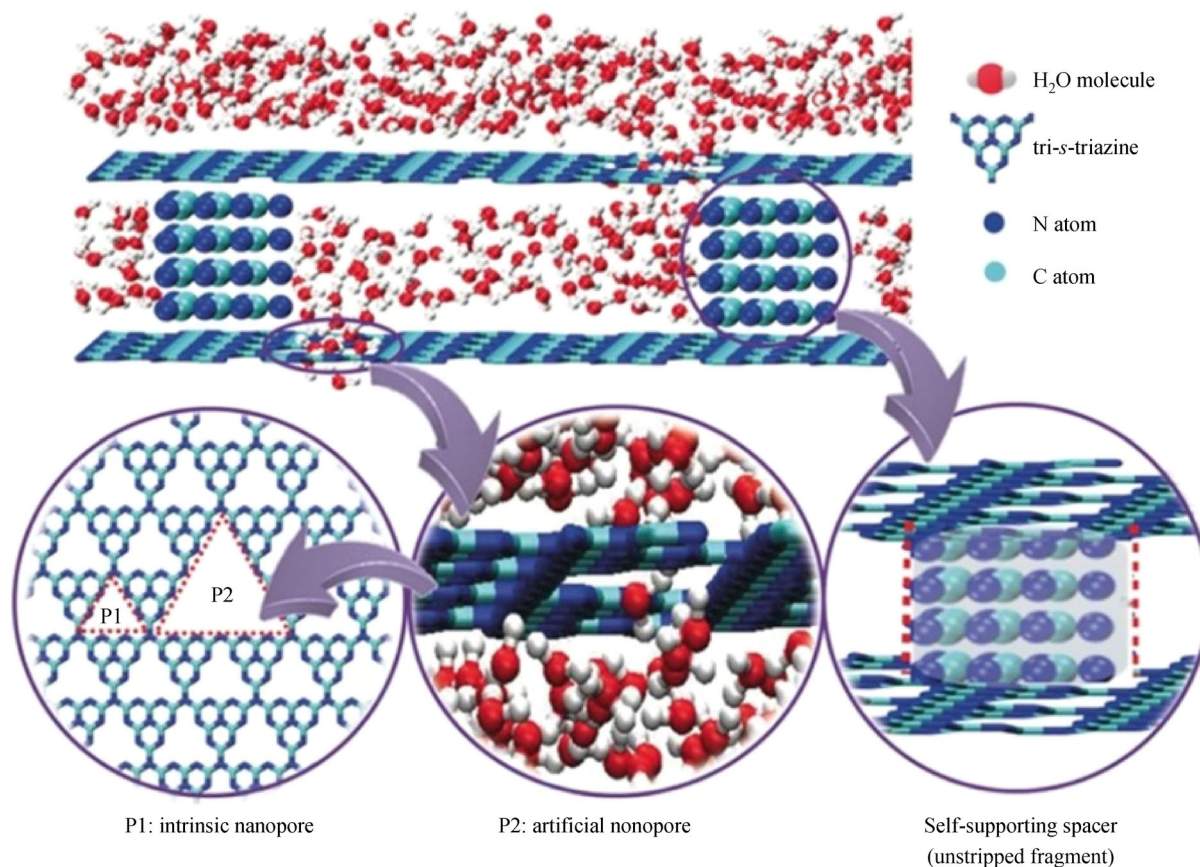


Fig. 6 Illustration of water transport through the $g-C_3N_4$ nanosheets-based membrane. Reprinted with permission from Ref. [26], copyright 2017 Wiley VCH.

impermeable to molecules (even helium gas molecules), making it unsuitable for any separation application [78]. However, many molecular simulations theoretically demonstrated that NPG held great potential in separation, especially water desalination [79], ion separation [80], and gas separation [81–88]. At first, great attention was paid to various perforation techniques such as focused electron beam drilling [89,90], focused ion beam irradiation [91], ion bombardment and chemical oxidative etching [92,93], ultraviolet-induced oxidative etching [94], and oxygen plasma etching [95] to perforate selective pores in graphene sheets to create NPG membranes. Several reviews dealing with this topic have compared the advantages and disadvantages of various perforation techniques [96,97]. Later, NPG membranes were also prepared by some other methods such as direct synthesis [98–100].

One of the major challenges in high-performance NPG membrane is the control of pore size. Huang et al. proposed an ozone functionalization-based etching and pore-modification chemistry to prepare membranes, and the resulting graphene membrane with smaller pore size and higher pore density displayed an increased H_2 permeance and an increased H_2/CH_4 selectivity [101]. Wang et al. used

molecular dynamics simulations to prove that the bilayer NPG membrane with the lateral shift of the two graphene layers can continuously tune the effective pore size [102]. Zhao et al. reported a partially decoupled defect nucleation and pore expansion to prepare the graphene membrane for highly efficient gas separations (Fig. 7(a)). The obtained membrane exhibited a good H_2/CH_4 selectivity (15.6 to 25.1), a good H_2/C_3H_8 selectivity (38.0 to 57.8), and a high H_2 permeance (1340 to 6045 GPU) [103]. Recently, Sun et al. theoretically demonstrated that the nonselective large pores can be tuned to the selective pores via adding charges on the graphene surfaces. Because of electrostatic interactions between CO_2 and the surface charges, the graphene nanopore with surface charges displayed increased CO_2/N_2 selectivity [104]. Moreover, larger graphene nanosheets almost inevitably have more defects. In order to utilize the polymer coatings to eliminate defects of membranes, Choi et al. fabricated the 20-nm-thick graphene-polymer hybrid membrane by a vapor-liquid interfacial polymerization process [105]. Yang et al. fabricated an ultrathin graphene-nanomesh (GNM)/single-walled carbon nanotube (SWNT) hybrid membrane with excellent mechanical strength (Fig. 7(b)). In this structure, the SWNT network with high mechanical strength served as a microscopic

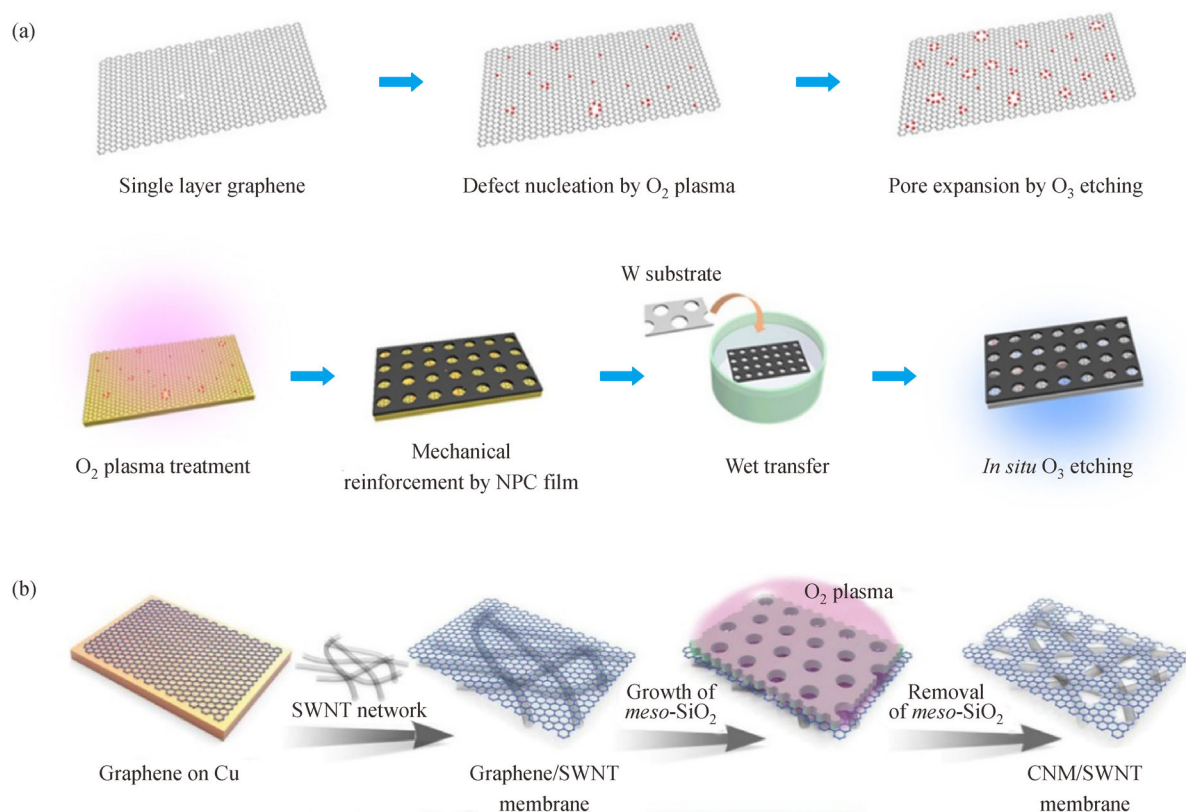


Fig. 7 (a) Illustration of the partially decoupled defect nucleation and pore expansion to prepare NPG membranes. Reprinted with permission from Ref. [103], copyright 2019 American Association for the Advancement of Science; (b) Schematic illustration of GNM/SWNT membranes fabrication. Reprinted with permission from Ref. [106], copyright 2019 American Association for the Advancement of Science.

framework to support the GNM, preventing the hybrid membrane from tearing and solute leakage during the efficient water purification over large areas [106].

4.2 2D membranes based on non-porous nanosheets

4.2.1 GO and reduced GO membranes

Among the graphene-based material family, besides NPG, more and more attentions have been paid to GO and reduced GO (rGO) for membrane separation. As the most widely studied graphene-based material for membrane separation, GO with oxygen-containing groups can be easily dispersed in water and enhance interactions with transport components. rGO can be obtained when oxygen atoms are removed from GO by reduction such as thermal reduction, chemical reduction, and solvothermal reduction. During the reduction process, defects could be formed in rGO, serving as nanopores to provide selective separations. To date, several articles about molecular simulations of GO- and rGO-based membranes have provided useful guidelines and directions for the preparation of high-performance separation membranes [107–110]. The following part will introduce recent advances in GO and rGO as 2D membrane materials for molecular and ionic separations.

In 2012, Nair et al. reported that the GO membranes were impermeable to liquids, vapors and gases, but allowed water to permeate unimpeded, making them promising for selective removal of water [111]. However, pure GO membranes are unstable in water environment. Hence, improving their performance stability for long-term membrane operation is very important. To solve this problem, much attention has been paid to the modification of GO by cross-linking, which can improve the water stability of GO membranes and control the charges, functionality, and spacing of the GO nanosheets. Different types of crosslinkers such as metal ions [112–114], polymers [5,115–117], and multifunctional small molecules [118–121] were used in the cross-linking process for membrane separation. Recently, Liang et al. achieved interlayer cross-linking by introducing sodium 1,4-phenylenediamine-2-sulfonate as the water transport promoters between GO nanosheets. The obtained membrane with a more stable structure and water transport promoters possessed a flux of $5.94 \text{ kg} \cdot \text{m}^{-2} \cdot \text{h}^{-1}$ accompanied by a separation factor of 3965 for water/butanol [122]. More recently, Pan et al. designed the GO membranes with dual crosslinkers, where polyvinylamine (PVAm) was used as the first crosslinker and silica generated from the biomineralization of PVAm served as the second crosslinker. The resulting GO-PVAm-silica membrane with a fixed interlayer spacing demonstrated a flux of $12.9 \pm 0.3 \text{ kg} \cdot \text{m}^{-2} \cdot \text{h}^{-1}$ and a separation factor of 1188 ± 39 for

water/butanol [123]. Nie et al. designed small-flake GO (SFGO) membranes with La^{3+} serving as a cross-linker and spacer. The resulting SFGO- La^{3+} membrane with shorter transport pathways of small-flake GO and a larger interlayer spacing could keep methanol permeance $> 100 \text{ L} \cdot \text{m}^{-2} \cdot \text{h}^{-1} \cdot \text{bar}^{-1}$ for 24 h under 3-bar pressure [13]. Besides, reducing GO nanosheets is effective in protecting membranes from swelling, which can improve the stability of GO membranes [124]. Huang et al. reported solvent solvated rGO membranes with high performance for the organic solvent nanofiltration, which was stable in organic solvents, and strong acidic, alkaline, or oxidative media [125].

In order to achieve better membrane separation, extensive effort has been focused on controlling the interlayer spacing in GO membrane. Creating more space and channels between layers always lead to a considerably enhanced membrane permeance. A widely adopted method to expand interlayer spacing is to introduce nano-sized spacers such as copper hydroxide nanostrands [126], nanoparticles [127–129], carbon nanodots [130], nanorods [131] and nanotubes [132–134] into the interlayers. For instance, Han et al. prepared a GO-based membrane intercalated with TiO_2 nanoparticles generated from the oxidation of lamellar MXene. Compared to the traditional intercalation method, MXene served as a sacrificial template to generate continuous water nanochannels because of the consecutive distribution of TiO_2 nanoparticles. The resulting membrane demonstrated a water permeability of $89.6 \text{ L} \cdot \text{m}^{-2} \cdot \text{h}^{-1} \cdot \text{bar}^{-1}$ with a rejection rate over 97% for four different organic dyes, Rhodamine B, methylene blue, crystal violet and neutral red [135]. Recently, Yu et al. designed a 2D-2D rGO- TiO_2 nanochannel membrane with TiO_2 nanosheets on an rGO template via a solvothermal-induced assembly method, and the resulting rGO- TiO_2 membrane exhibited a permeance of $9.82 \text{ L} \cdot \text{m}^{-2} \cdot \text{h}^{-1} \cdot \text{bar}^{-1}$ accompanied by a rejection rate of 98.5% for RhB [136]. Moreover, the typical reduction of GO to rGO is a useful way to control the interlayer spacing. Han et al. designed ultrathin rGO membranes with well packed layer structure, which possessed a water permeance of $21.8 \text{ L} \cdot \text{m}^{-2} \cdot \text{h}^{-1} \cdot \text{bar}^{-1}$ with a rejection rate of 99.2% for methyl blue [137].

Some 2D materials including MoS_2 [138], WS_2 [139], MXene [140,141] and niobate nanosheets [142] have also been combined with GO nanosheets to construct hybrid 2D laminar membranes. For example, Endo et al. fabricated GO/few-layer graphene hybrid 2D membranes followed by thermal treatment and Ca^{2+} crosslinking. The obtained GO/FLG membrane showed a steady performance (NaCl rejection of 85% and acid blue 9 rejection of 96%) for up to 120 h under intense cross-flow [143]. As for gas separation of GO membranes, Kim et al. reported that gas transport behavior of layered GO membranes can be controlled via different stacking methods in 2013 [144]. Simultaneously,

Li et al. prepared 1.8 nm-thick GO membranes with an H_2/CO_2 selectivity of 3400 accompanied by an H_2/N_2 selectivity of 900 via a facile filtration process [14]. Encouraged by this success, GO membranes have also been considered as a promising candidate for gas separation. However, controlling the nanochannels/sub-nanochannels in GO membrane is also a challenge for their application in gas separation. For example, Shen et al. reported a facile external force driven assembly strategy to prepare GO membrane with an interlayer height of ~ 0.4 nm via the synergistic manipulation of “outer” and “inner” external forces (Fig. 8) [5].

In biological membranes, precise molecule separation not only can be realized by the molecular sieving relying on the size of nanochannels, but also can be realized by facilitated target molecule transport relying on carriers fixed in the nanochannel surfaces. Recently, inspired by dual transport mechanisms of biological membranes, Dou et al. designed Ag/IL-GO membranes with silver ions served as ethylene transport carrier and ionic liquid (IL) tuning the size of nanochannels. Owing to the cooperative effect of the in-plane molecular sieving and plane-to-plane carrier-facilitated transport, the obtained membrane showed a good C_2H_4 permeance of 72.5 GPU accompanied by a selectivity of 215 for $\text{C}_2\text{H}_4/\text{C}_2\text{H}_6$ (Fig. 9(a)) [145].

2D membranes have good chemical and thermal stability, and their nanoscale-thickness makes the water permeation rate very high, which can be used in the

treatment of wastewater. In order to realize high separation performance for nanofiltration process, attention should be focused on the design and strategies employed to control interlayer spacing to enhance permeability and selectivity. Besides, the high-quality nanosheets with high yield, and assembling them to 2D membranes with refined structure as designed, as well as the nanofiltration device also have effect on the separation performance. Inspired by the charge interaction in biological membranes, Zhang et al. created surface charges on GO membrane to control ion transport. Owing to the high repulsive interaction, the obtained highly charged GO membrane repelled doubly charged ions, possessing the same charge of the membrane surface. Meanwhile, in order to balance the overall solution charge, the obtained highly charged GO membrane also restrained the permeation of singly charged ions, possessing the opposite charge of the membrane surface (Fig. 9(b)). Therefore, the resulting membrane could separate AB_2 - or A_2B -type salts from water, while simultaneously maintaining a high water flux [15]. More recently, Wen et al. reported a planar heterogeneous interface desalination of a planar heterogeneous graphene oxide membrane (PHGOM) with a NaCl rejection rate of 97.0%, but a water flux of $1529 \text{ L}\cdot\text{m}^{-2}\cdot\text{h}^{-1}\cdot\text{bar}^{-1}$. The PHGOM was prepared via the dual-flow filtration with a clapboard to separate negatively charged GO nanosheets and positively charged GO nanosheets (Fig. 9(c)). In the presence of an electric field, the ion transport behavior of the sodium and chloride resulted in a salt concentration

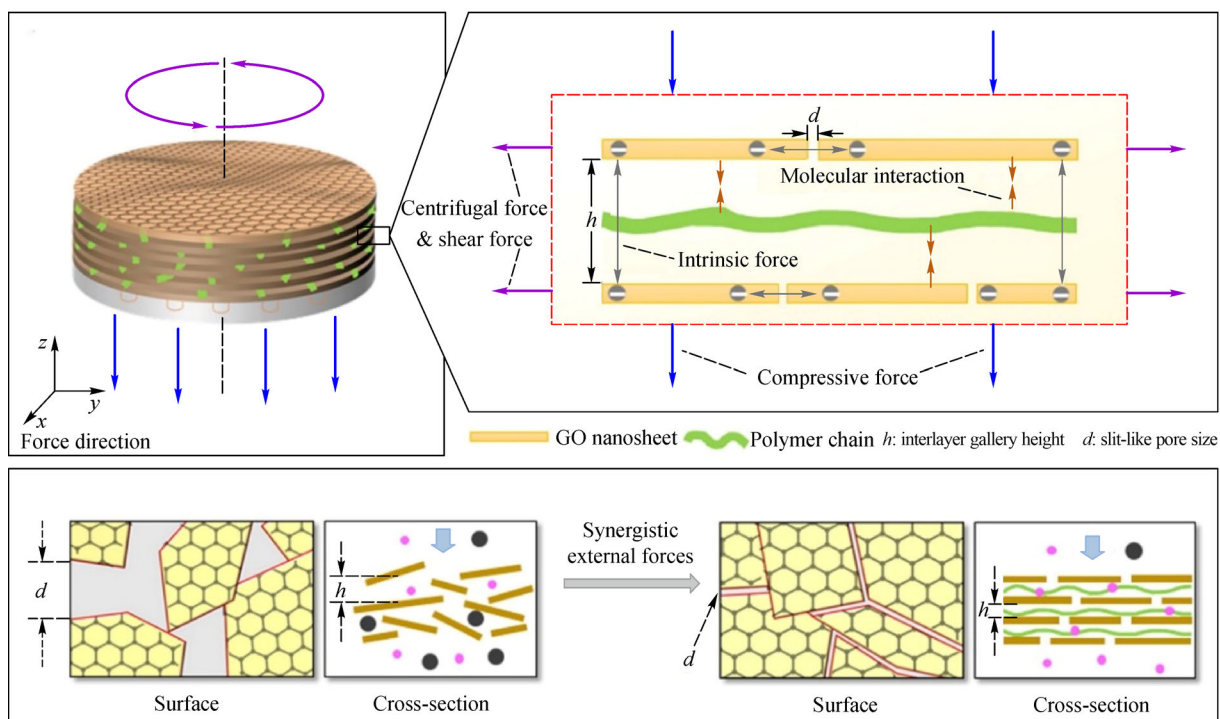


Fig. 8 External force driven assembly strategy for the fabrication of GO membranes. Reprinted with permission from Ref. [5], copyright 2016 American Chemical Society.

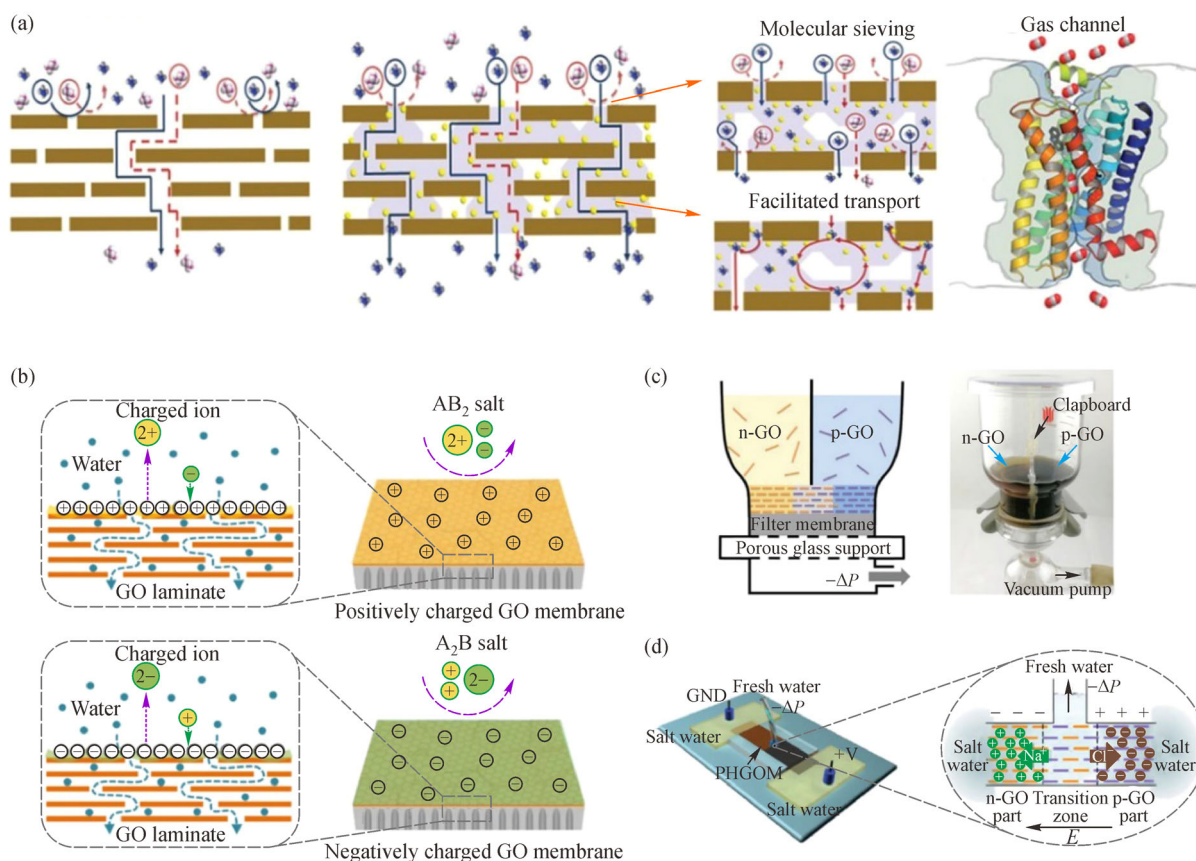


Fig. 9 (a) Synergistic effects of molecular sieving and carrier-facilitated transport by imitating biological protein nanochannels. Reprinted with permission from Ref. [145], copyright 2019 John Wiley and Sons; (b) Schematic of the design of surface-charged GO membranes. Reprinted with permission from Ref. [15], copyright 2019 Nature Publishing Group; (c) Scheme illustration of the preparation of the PHGOM. (d) Scheme of the working mechanism of a PHGOM-based device for water desalination. Reprinted with permission from Ref. [146], copyright 2020 Wiley VCH.

depletion state transition zone, and thus deionized water can be extracted from the transition zone via an inverted T-shaped water extraction mode (Fig. 9(d)) [146]. PHGOM membrane exhibited good salt rejection with ultrahigh water flux, almost two or three orders of magnitude higher than other 2D membranes. Compared with the GO membrane [15], the composite GO-PVAm-silica membrane [123] present higher water flux and higher ion rejection due to the specially designed structure. In addition to the manipulation of the interlayer spacing and improving membrane performance stability, special attention should also be focused on the design of the desalination device to enhance permeation and selectivity for desalination processes.

4.2.2 LDH membranes

LDHs, as a representative of anionic clays, are formed by positively charged layers and interlayer galleries containing charge-compensating anions [147]. In 2008, Kim et al. prepared the LDH thin films via electrophoretic deposition

method, exhibiting slight permselective property toward CO_2 [148]. Then, they prepared $MgAl-CO_3$ LDH membranes by a vacuum-suction method. In order to reduce voids and pinholes in the membranes, the obtained LDH membrane was repaired by silicone coating, exhibiting a CO_2/N_2 selectivity of 34.4 [149]. In 2014, Caro's group fabricated $NiAl-CO_3$ LDH membranes via the *in situ* hydrothermal growth, realizing an H_2/CH_4 separation factor of 80 [150]. Recently, Liu et al. reported 2D LDH membranes with inherent CO_2 -selective transport channels. Owing to the intrinsic breathing effect of LDH toward CO_2 , the intercalated CO_3^{2-} ions transformed from CO_2 regulated the channel from 0.7 nm to 0.3 nm by electrostatic interaction with LDH layers, endowing the resulting membrane with a good separation performance for CO_2/CH_4 [151]. Furthermore, Caro's group designed a ZIF-8@ $MgAl-CO_3$ LDH membrane, introducing a new concept of "LDH buffer layer". First, vertically aligned $MgAl-CO_3$ LDH layers were fixed on substrates. Then, ZIF-8 seeds were deposited on $MgAl-CO_3$ LDH layers, which could prevent ZIF-8 seeds from falling off

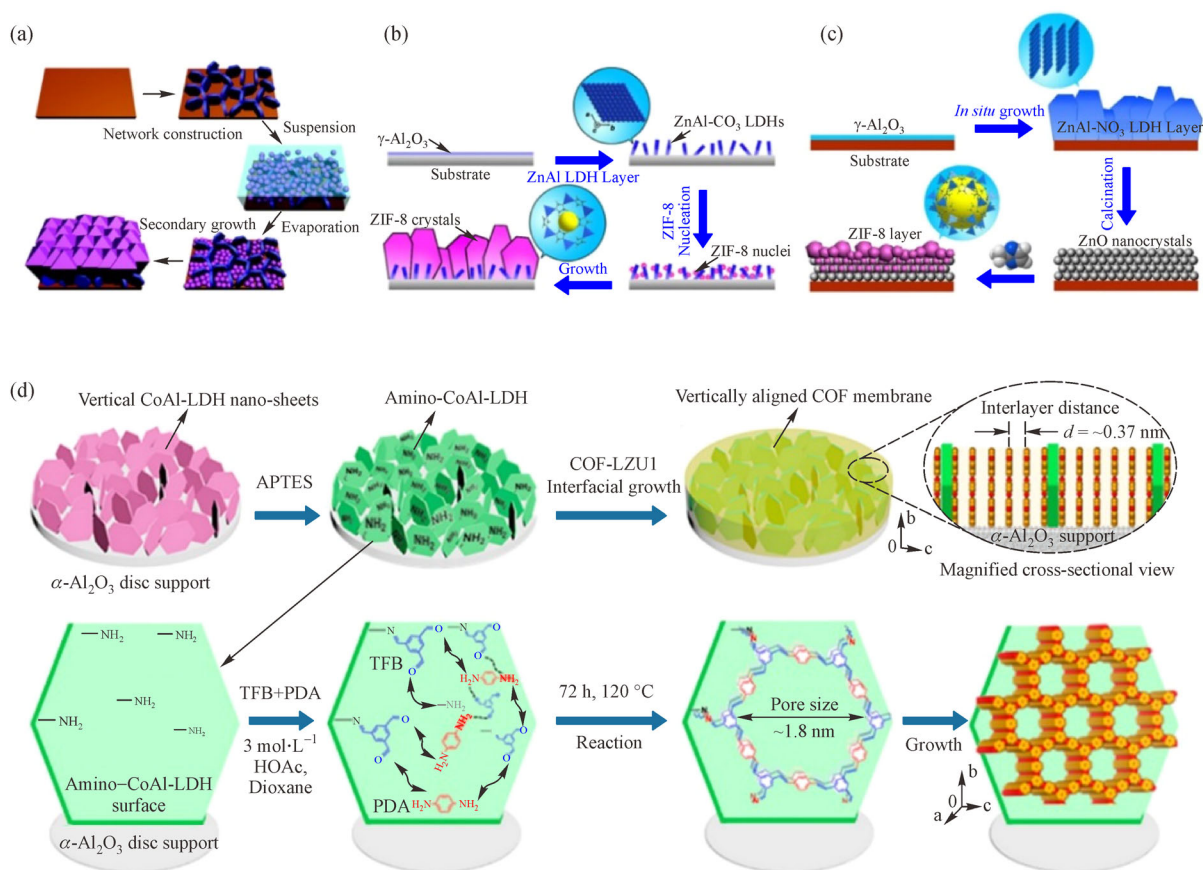


Fig. 10 (a) The formation of ZIF-8 membranes on vertically aligned MgAl-CO₃ LDH layers. Reprinted with permission from Ref. [152], copyright 2014 The Royal Society of Chemistry; (b) The formation of ZIF-8 membranes on ZnAl-CO₃ LDH buffer layers. Reprinted with permission from Ref. [153], copyright 2014 American Chemical Society; (c) The formation of ZIF-8 membranes via partial conversion of a ZnO buffer layer from a ZnAl-NO₃ LDH layer. Reprinted with permission from Ref. [154], copyright 2015 Wiley VCH; (d) Illustration of the vertically aligned COF membrane formation. Reprinted with permission from Ref. [155], copyright 2020 American Chemical Society.

(Fig. 10(a)). Finally, the ZIF-8@MgAl-CO₃ LDH membrane with an H₂/CH₄ separation factor of 12.9 accompanied by an H₂ permeance of $1.4 \times 10^{-7} \text{ mol} \cdot \text{m}^{-2} \cdot \text{s}^{-1} \cdot \text{Pa}^{-1}$ was achieved via secondary growth [152]. Furthermore, Caro's group further prepared vertically aligned ZnAl-CO₃ LDH buffer layers on substrates via *in situ* solvothermal growth by the urea hydrolysis method (Fig. 10(b)). Contrary to the physical interaction between ZIF-8 and MgAl-CO₃ LDH network, this work reported the high-affinity metal-imidazole interaction between ZnAl-CO₃ LDHs and ZIF-8 crystals, where ZIF-8 membranes can be directly synthesized on the ZnAl-CO₃ LDHs. The as-prepared composite membrane demonstrated an H₂/CH₄ separation factor of 12.5 with an H₂ permeance of $1.4 \times 10^{-7} \text{ mol} \cdot \text{m}^{-2} \cdot \text{s}^{-1} \cdot \text{Pa}^{-1}$ [153]. In order to further improve the gas selectivity of ZIF-8@ZnAl-NO₃ LDH composite membrane, Caro's group used the controlled calcination of a ZnAl-NO₃ LDH membrane to create a ZnO buffer layer, which was

subsequently turned into ZIF-8 membrane through a solvothermal treatment with the mixed H₂O/DMF solution containing ligand of 2-methylimidazole (Fig. 10(c)). The obtained ultra-thin membrane exhibited an excellent H₂/CH₄ separation factor of 83.1 accompanied by an H₂ permeance of $1.9 \times 10^{-8} \text{ mol} \cdot \text{m}^{-2} \cdot \text{s}^{-1} \cdot \text{Pa}^{-1}$ [154]. Recently, Caro's group designed COF-in-LDH membranes via *in situ* growth of 2D COF (COF-LZU1 or TFB-BD) on vertically aligned CoAl-LDH nanosheets (Fig. 10(d)). In contrast to 2D COF membranes based on intrinsic pore sieving, the separation of the as-obtained membrane was mainly based on the COF interlayer space. The obtained COF-LZU1 membrane demonstrated an H₂ permeance of 3655 GPU accompanied by an H₂/CO₂ selectivity of 31.6 [155].

Besides gas separation, LDH-based membranes have received increasing attention for liquid separation [156–159]. For example, Wang et al. prepared an intercalated MgAl-LDH membrane intercalated with amino acids on

porous tubes via an *in situ* hydrothermal process. The glycine-intercalated LDH composite membrane possessed a water permeance of $566 \text{ L} \cdot \text{m}^{-2} \cdot \text{h}^{-1} \cdot \text{MPa}^{-1}$ with a rejection rate of 98.5% for Eriochrome Black T molecules [160]. Recently, as revealed by Ang et al., the solvent permeation of LDH membranes improved by altering the divalent cation in the LDH crystal structure, providing preliminary guidelines for their application as organic solvent nanofiltration membranes [161].

4.2.3 MXene membranes

Transition metal carbides and/or nitrides, named MXenes, were first reported by Gogotsi's and Barsoum's groups [162,163]. As a family of emerging 2D materials, MXene nanosheets are similar to GO nanosheets and can be used into 2D membranes for size-selective separations. $\text{Ti}_3\text{C}_2\text{T}_x$ is one of the representative MXenes, usually prepared by a HF or HCl/LiF etching process. Gogotsi's group reported the very first example of 2D $\text{Ti}_3\text{C}_2\text{T}_x$ MXene membranes via a vacuum-assisted filtration with exfoliated 2D $\text{Ti}_3\text{C}_2\text{T}_x$ sheets. Because of the presence of H_2O between the hydrophilic $\text{Ti}_3\text{C}_2\text{T}_x$ layers, the obtained 2D $\text{Ti}_3\text{C}_2\text{T}_x$ membrane exhibited a water flux of $37.4 \text{ L} \cdot \text{m}^{-2} \cdot \text{h}^{-1} \cdot \text{bar}^{-1}$ [164]. Then, our group designed a 2D $\text{Ti}_3\text{C}_2\text{T}_x$ membrane with positively charged $\text{Fe}(\text{OH})_3$ colloidal nanocrystals serving as the distance holder to create expanded nanochannels followed by HCl dissolution (Fig. 11(a)). The obtained MXene membrane exhibited an excellent water permeance of $1084 \text{ L} \cdot \text{m}^{-2} \cdot \text{h}^{-1} \cdot \text{bar}^{-1}$ accompanied by an Evans blue rejection rate of 90% [16]. Besides liquid separation, our group also applied the MXene membranes to gas separation, exhibiting aligned and regular subnanochannels. The obtained membrane exhibited a good H_2/CO_2 selectivity > 160 with an H_2 permeability > 2200 Barrer [17]. Subsequently, Li et al. studied the gas transportation mechanism of different gas molecules in MXene membranes by MD simulations. The simulation results proved that the structure and interlayer spacing of MXene membrane were important for the gas diffusion [165]. Shen et al. achieved precise manipulation of stacking behaviors and interlayer spacing of MXene nanosheets by borate and polyethylenimine molecules [6]. Wang et al. designed 2D lamellar MXene membranes with regular and straight interlayer channels via the direct self-stacking of rigid MXene nanosheets. The resulting membrane with ordered 2 nm channels showed a precise molecular (larger than 2 nm) rejection and a water permeance of $2300 \text{ L} \cdot \text{m}^{-2} \cdot \text{h}^{-1} \cdot \text{bar}^{-1}$ [7]. Wu et al. applied hydrophilic ($-\text{NH}_2$) and hydrophobic ($-\text{C}_6\text{H}_5$, $-\text{C}_{12}\text{H}_{25}$) groups to tune the size and wettability of nanochannels. Compared to hydrophobic nanochannels with disordered molecular configuration, hydrophilic nanochannels with highly ordered alignment aggregates displayed better separation permeance. However, the permeance of the

nonpolar molecule was comparable in both hydrophilic and hydrophobic nanochannels [166]. Recently, Xing et al. adopted a freeze-drying method to directly synthesize the crumpled $\text{Ti}_3\text{C}_2\text{T}_x$ MXene nanosheets from flat $\text{Ti}_3\text{C}_2\text{T}_x$ MXene nanosheets for the fabrication of *c*- $\text{Ti}_3\text{C}_2\text{T}_x$ MXene membranes via vacuum filtration (Fig. 11(b)). The obtained *c*- $\text{Ti}_3\text{C}_2\text{T}_x$ MXene membrane with larger interlayer channels demonstrated ultrafast permeation for water and acetone [167]. Moreover, the swelling of MXene membranes in aqueous solution is still a challenge to overcome. Recently, our group fabricated non-swelling Al^{3+} -intercalated MXene membranes. Affinity interactions between Al^{3+} and the abundant oxygen functional groups terminating at the MXene surface made the non-swelling MXene membrane exhibit a long-term stability in liquid water up to 400 h with a water permeance of $2.8 \text{ L} \cdot \text{m}^{-2} \cdot \text{h}^{-1}$ and a rejection rate of 96.5% for NaCl [168]. Moreover, our group reported a self-crosslinked MXene membrane in the presence of Ti–O–Ti bonds for a stable interlayer spacing, which could improve the performance of ion exclusion and anti-swelling property [169].

Besides pure MXene membranes, MXene-based separation membranes have also received increasing attention. For instance, Wu et al. prepared $\text{Ti}_3\text{C}_2\text{T}_x/\text{PEI}$ and $\text{Ti}_3\text{C}_2\text{T}_x/\text{PDMS}$ MMMs. Compared to the pure polymer membranes, the alcohol fluxes of the as-obtained MMMs increased by 30% and 162%, respectively [170]. Then, Hao et al. further incorporated functionalized $\text{Ti}_3\text{C}_2\text{T}_x$ nanosheets with four types of groups into polymers. As a consequence, the obtained membrane with multi-functional $\text{Ti}_3\text{C}_2\text{T}_x$ nanosheets enhanced the fluxes [171]. More recently, Shamsabadi et al. introduced 2D $\text{Ti}_3\text{C}_2\text{T}_x$ MXene nanosheets into the Pebax-1657 to improve the separation performance [172]. Furthermore, Gao et al. reviewed a great deal of work about MXene/polymer membranes and provided perspectives and useful guidelines for the development of MXene/polymer membranes [173].

4.2.4 TMD membranes

2D TMDs are a new type of 2D layered materials, which have received intense attention after graphene. The general chemical formula of TMDs is MX_2 , where M is the transition metal element and X represents chalcogen. Many molecular simulations showed a bright prospect of TMD materials for membrane-based separation, especially MoS_2 nanosheets and WS_2 nanosheets [174–176]. Sun et al. reported the first example of laminar MoS_2 membranes with a water permeance of $245 \text{ L} \cdot \text{m}^{-2} \cdot \text{h}^{-1} \cdot \text{bar}^{-1}$ accompanied by an Evans blue rejection rate of 89% by the assembly of atom-thick MoS_2 sheets [177]. Then, they also prepared 2D nanostrands-channelled WS_2 membranes via filtering the nanostrands/ WS_2 nanosheet suspension on the porous AAO substrates. Notably, they found that the nanochannels created by the ultrathin nanostrands between

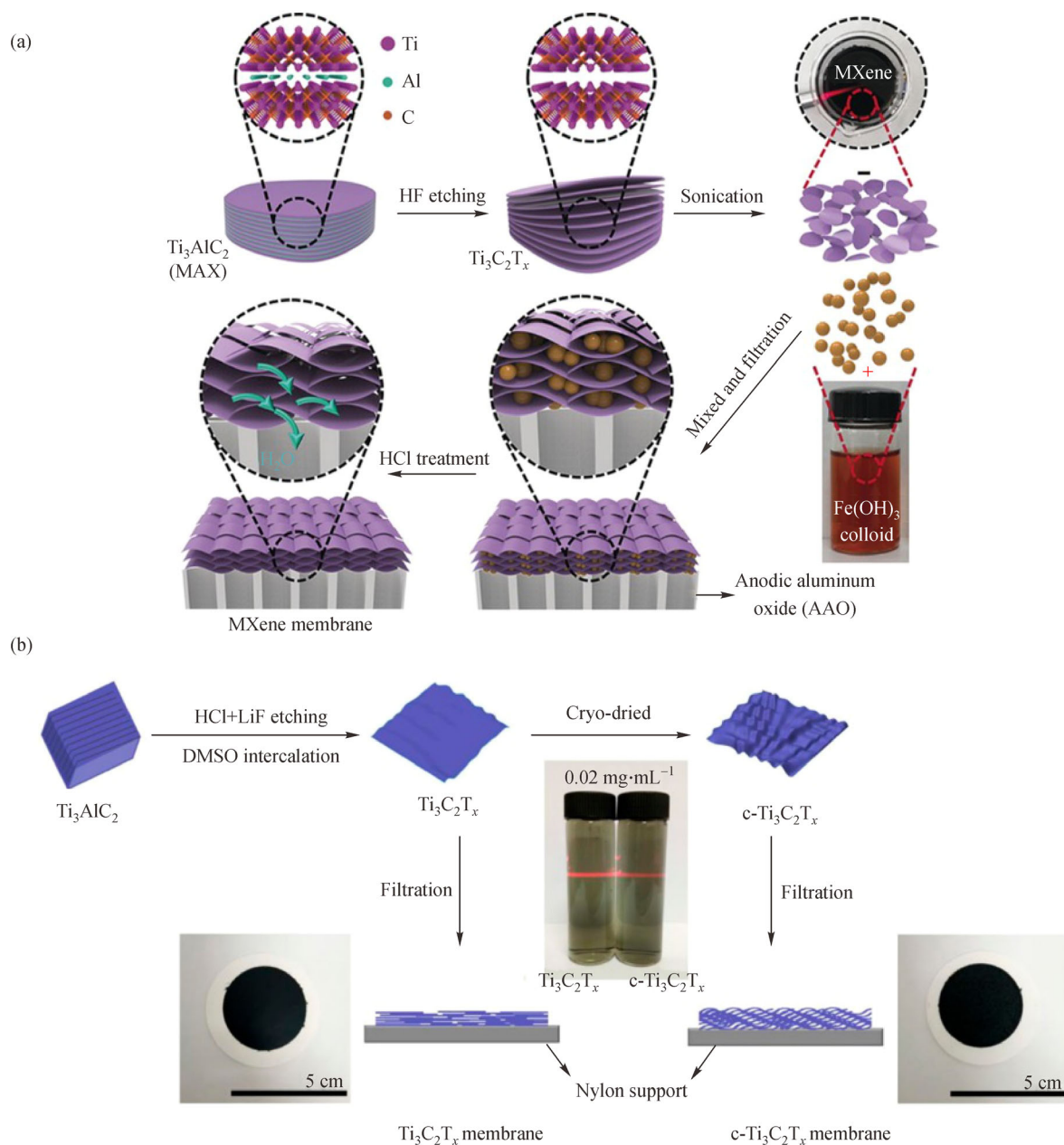


Fig. 11 (a) The preparation of MXene membranes with $\text{Fe}(\text{OH})_3$ served as distance holder. Reprinted with permission from Ref. [16], copyright 2017 Wiley VCH. (b) The fabrication of $\text{Ti}_3\text{C}_2\text{T}_x$ membranes and $c\text{-Ti}_3\text{C}_2\text{T}_x$ membranes. Reprinted with permission from Ref. [167], copyright 2020 American Chemical Society.

the WS_2 sheets cracked under high pressure. Owing to the new fluidic nanochannels created by the crack, the obtained membrane showed an increase in the flux without a markedly reduced rejection for Evans blue [178]. Motivated by their work, this topic received increasing attention. In order to improve the separation performance, Hirunpinyopas et al. proposed a chemical dye functionalization strategy to protect membranes from swelling when exposed to the water environment. The main procedure is to filter exfoliated MoS_2 dispersion on a PVDF membrane

and subsequently immerse in the dye solution. The resulting membrane showed a good stability without swelling in water for periods exceeding 6 months [179]. Ang et al. used cationic LDH nanosheets to control the interlayer spacing of anionic TMD nanosheets, and the obtained membrane displayed almost 100% rejection of methyl orange, dissolved in acetone [180]. In addition, Ries et al. reported the covalently functionalized molybdenum disulfide (MoS_2) nanosheets to prepare the 2D MoS_2 membranes with different functional groups.

Modification with different functional groups could not only control the interlayer spacing, but also control the surface chemistry of 2D MoS₂ membranes. The acetamide-functionalized 2D MoS₂ membrane demonstrated a water flux of 33.7 L·m⁻²·h⁻¹·bar⁻¹ accompanied by a NaCl rejection of 82% [181].

In addition to the widely used solvent-exfoliation method to prepare nanosheets, Li et al. successfully prepared 7 nm-thick 2D MoS₂ membranes via the integration of chemical vapor deposition-grown centimeter-scale nanosheets onto porous polymeric substrates (Fig. 12). The obtained ultrathin membrane displayed a water permeance of 322 L·m⁻²·h⁻¹·bar⁻¹ accompanied by the ion rejection rates of 99% for various seawater salts including Na⁺, K⁺, Ca²⁺ and Mg²⁺ [18]. Owing to the high-quality nanosheets and assembling them to 2D membranes with refined structure as designed, such atom-thick membrane made from chemical vapor deposition showed a ultrahigh water permeance with excellent ionic sieving capability compared to other 2D MoS₂ membranes made from exfoliated nanosheets reported by Ries et al. [181]. Recently, Hu et al. designed tannic acid-modified MoS₂ nanosheets via a tannic acid assisted exfoliation method. The obtained hybrid membrane with 1 wt% TAMoS₂ in MoS₂ membrane displayed a water flux of 10000 L·m⁻²·h⁻¹·bar⁻¹ accompanied by a rejection of 98% for methylene blue [182].

Although TMD membranes are often used for liquid separation, a growing number of articles have been published on TMDs membranes for gas separation. In 2015, Wang et al. prepared the first example of ultrathin 2D MoS₂ membranes via a simple filtration for the gas separation. Owing to the presence of the larger stacking space, the gas transportation in 17 nm-thick MoS₂ membranes present a Knudsen diffusion behavior, and the obtained membrane demonstrated a high H₂ permeance of 27440 GPU but a poor H₂/CO₂ selectivity (~3) [183]. Then, Achari et al. prepared 500 nm-thick MoS₂

membranes with an H₂ permeability of 1175 Barrer and an H₂/CO₂ selectivity of 8.29. They also discovered a phase transition of MoS₂ via heating at 160 °C, inducing the decrease of membrane interlayer spacing from 11.32 to 6.12 Å and consequent enhancement (30%) in H₂ permeability of the membranes without reducing the selectivity [184]. Shen et al. designed a composite MMM via a simple drop-coating and evaporation method. The resulting MoS₂-Pebax/PDMS/PSf membrane possessed a CO₂ permeability of 64 Barrer accompanied by a CO₂/N₂ selectivity of 93 [185]. Moreover, Chen et al. reported that 1-butyl-3-methylimidazolium tetrafluoroborate IL was confined into the channels of MoS₂ membranes and WS₂ membranes via infiltration. Owing to the high CO₂ solubility of the IL, membranes with the nanoconfined IL exhibited a good CO₂ permeance and excellent CO₂/gas selectivities [19,186].

Tables 1 and 2 summarize detailed fabrication approaches of various 2D-material membranes mentioned in this review.

5 Challenges and perspectives

2D membranes, as the most promising family of separation membranes, have received increasing attention in recent years. The nanostructures/subnanostructures and micro-environments of nanopores and/or nanochannels have been tuned by ion/molecule intercalation, interlayer cross-linking, and charge modification, resulting in promising 2D membranes with precise molecular sieving. Besides, the ultrathin 2D membranes would greatly shorten the molecule transport pathway, minimizing mass-transfer resistance and thus increasing membrane permeance, while simultaneously maintaining a high selectivity, surpassing the upper bound of the separation performance of traditional membranes.

As summarized in Tables 1 and 2, even with significant

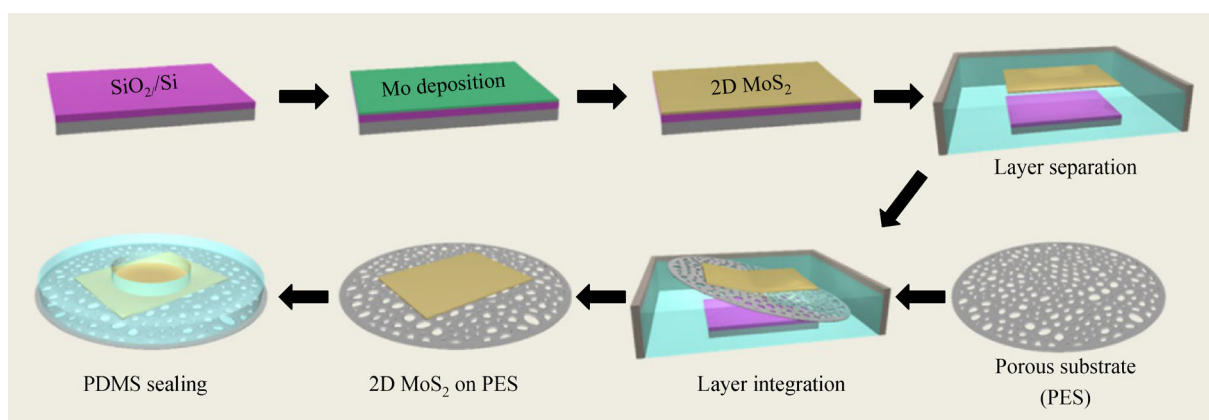


Fig. 12 The fabrication of ultrathin 2D MoS₂ membranes. Reprinted with permission from Ref. [18], copyright 2019 American Chemical Society.

Table 1 Summary of gas separation for 2D-material membranes

Feed condition	Membrane	Fabrication approach	Permeability/permeance (of faster species)	Selectivity	Ref.
<i>p</i> -Xylene/ <i>o</i> -xylene	MFI	Secondary growth	$4 \times 10^{-7} \text{ mol} \cdot \text{m}^{-2} \cdot \text{s}^{-1} \cdot \text{Pa}^{-1}$	25–45	[32]
<i>p</i> -Xylene/ <i>o</i> -xylene	Silicalite-1	Gel-free secondary growth	$1.3 \times 10^{-7} \text{ mol} \cdot \text{m}^{-2} \cdot \text{s}^{-1} \cdot \text{Pa}^{-1}$	1050	[33]
<i>p</i> -Xylene/ <i>o</i> -xylene	MFI	Gel-free secondary growth	$2.4 \times 10^{-7} \text{ mol} \cdot \text{m}^{-2} \cdot \text{s}^{-1} \cdot \text{Pa}^{-1}$	500	[34]
<i>p</i> -Xylene/ <i>o</i> -xylene	MFI	Gel-free secondary growth	$5.6 \times 10^{-7} \text{ mol} \cdot \text{m}^{-2} \cdot \text{s}^{-1} \cdot \text{Pa}^{-1}$	2000	[35]
<i>p</i> -Xylene/ <i>o</i> -xylene	MFI	Gel-free secondary growth	$2.9 \times 10^{-7} \text{ mol} \cdot \text{m}^{-2} \cdot \text{s}^{-1} \cdot \text{Pa}^{-1}$	> 10000	[20]
H ₂ /CO ₂	AMH-3/PBI	Casting	1 Barrer	35	[39]
H ₂ /CO ₂	Zn ₂ (bim) ₄	Hot-drop coating	2700 GPU	291	[4]
H ₂ /CO ₂	Zn ₂ (bim) ₃	Hot-drop coating	$8 \times 10^{-7} \text{ mol} \cdot \text{m}^{-2} \cdot \text{s}^{-1} \cdot \text{Pa}^{-1}$	166	[22]
H ₂ /CO ₂	CuBDC-GO	Vacuum filtration	$9.6 \times 10^{-7} \text{ mol} \cdot \text{m}^{-2} \cdot \text{s}^{-1} \cdot \text{Pa}^{-1}$	95.1	[52]
H ₂ /CO ₂	Zn ₂ (bim) ₄ /GO	Direct growth	$1.4 \times 10^{-7} \text{ mol} \cdot \text{m}^{-2} \cdot \text{s}^{-1} \cdot \text{Pa}^{-1}$	106	[55]
H ₂ /CO ₂	MAMS-1	Hot-drop coating	553±228 GPU	235±14	[23]
H ₂ /CO ₂	[Cu ₂ (ndc) ₂ (dabco)]n/PBI	Casting	6.13±0.03 Barrer	26.7	[49]
H ₂ /CO ₂	Zn ₂ (bim) ₄	Direct growth	$2.04 \times 10^{-7} \text{ mol} \cdot \text{m}^{-2} \cdot \text{s}^{-1} \cdot \text{Pa}^{-1}$	53	[56]
H ₂ /N ₂				67	
H ₂ /CH ₄				90	
H ₂ /CO ₂	Co ₂ (bim) ₄	Vapor phase transformation	$1.72 \times 10^{-7} \text{ mol} \cdot \text{m}^{-2} \cdot \text{s}^{-1} \cdot \text{Pa}^{-1}$	58.7	[57]
H ₂ /CO ₂	<i>c</i> -Oriented ZIF-L	Secondary growth	$1.95 \times 10^{-7} \text{ mol} \cdot \text{m}^{-2} \cdot \text{s}^{-1} \cdot \text{Pa}^{-1}$	24.3	[53]
H ₂ /CO ₂	MXene	Vacuum filtration	2226.6 Barrer	167	[17]
H ₂ /CO ₂	Polyimide-PGM	Vapor-liquid interfacial polymerization	$6.85 \times 10^{-6} \text{ mol} \cdot \text{m}^{-2} \cdot \text{s}^{-1} \cdot \text{Pa}^{-1}$	6.41	[105]
H ₂ /CO ₂	TpEBr@TpPa-SO ₃ Na	Layer-by-layer assembly	2566 GPU	22.6	[25]
H ₂ /CO ₂	COF-LZU1	<i>In situ</i> growth	3654.8 GPU	31.6	[155]
H ₂ /CO ₂	COF-LZU1-ACOF-1	Temperature-swing solvothermal approach	$2.24 \times 10^{-7} \text{ mol} \cdot \text{m}^{-2} \cdot \text{s}^{-1} \cdot \text{Pa}^{-1}$	24.2	[65]
H ₂ /N ₂			$2.38 \times 10^{-7} \text{ mol} \cdot \text{m}^{-2} \cdot \text{s}^{-1} \cdot \text{Pa}^{-1}$	83.9	
H ₂ /CH ₄			$1.82 \times 10^{-7} \text{ mol} \cdot \text{m}^{-2} \cdot \text{s}^{-1} \cdot \text{Pa}^{-1}$	100.2	
H ₂ /CO ₂	GO	Vacuum filtration	$10^{-7} \text{ mol} \cdot \text{m}^{-2} \cdot \text{s}^{-1} \cdot \text{Pa}^{-1}$	3400	[14]
H ₂ /N ₂				900	
H ₂ /CO ₂	EFDA-GO	External force driven assembly	840–1200 Barrer	29–33	[5]
H ₂ /C ₃ H ₈			$3.9 \times 10^{-7} \text{ mol} \cdot \text{m}^{-2} \cdot \text{s}^{-1} \cdot \text{Pa}^{-1}$	260	
H ₂ /N ₂	MCM-22/Silica	Layer-by-layer deposition	$2.09 \times 10^{-8} \text{ mol} \cdot \text{m}^{-2} \cdot \text{s}^{-1} \cdot \text{Pa}^{-1}$	7.5	[37]
H ₂ /N ₂	MCM-22/Silica	Deposition cycles	$10^{-8} \text{ mol} \cdot \text{m}^{-2} \cdot \text{s}^{-1} \cdot \text{Pa}^{-1}$	> 100	[38]
H ₂ /CH ₄	JDF-L1/6FDA-4MPD + 6FDA-DABA	Casting	137±14 Barrer	35.6±1.4	[41]
H ₂ /CH ₄	JDF-L1/polysulfone	Casting	12.5 Barrer	128±13	[42]
H ₂ /CH ₄	MCM-41 + JDF-L1/6FDA-4MPD + 6FDA-DABA	Casting	440 Barrer	32	[43]
H ₂ /CH ₄	NiAl-CO ₃ LDH	<i>In situ</i> growth	$4.5 \times 10^{-8} \text{ mol} \cdot \text{m}^{-2} \cdot \text{s}^{-1} \cdot \text{Pa}^{-1}$	78	[150]
H ₂ /CH ₄	ZIF-8@MgAl-CO ₃ LDH	<i>In situ</i> growth Secondary growth	$1.4 \times 10^{-7} \text{ mol} \cdot \text{m}^{-2} \cdot \text{s}^{-1} \cdot \text{Pa}^{-1}$	12.9	[152]
H ₂ /CH ₄	ZIF-8@ZnAl-CO ₃ LDH	<i>In situ</i> growth	$1.4 \times 10^{-7} \text{ mol} \cdot \text{m}^{-2} \cdot \text{s}^{-1} \cdot \text{Pa}^{-1}$	12.5	[153]
H ₂ /CH ₄	ZIF-8@ZnAl-CO ₃ LDH	<i>In situ</i> growth	$1.9 \times 10^{-8} \text{ mol} \cdot \text{m}^{-2} \cdot \text{s}^{-1} \cdot \text{Pa}^{-1}$	83.1	[154]
H ₂ /CH ₄	Porous graphene	LPCVD	6045 GPU	15.6	[103]
CO ₂ /CH ₄	AMH-3/cellulose acetate	Casting	10.36±0.25 Barrer	30.03±0.34	[40]
CO ₂ /CH ₄	CuBDC/PI	Casting	2.78±0.02 Barrer	88.2±1.3	[48]
CO ₂ /CH ₄	CuBDC/PIM-1	Casting	407.3 GPU	15.6	[50]

(Continued)

Feed condition	Membrane	Fabrication approach	Permeability/permeance (of faster species)	Selectivity	Ref.
CO ₂ /CH ₄	CuBDC/6FDA-DAM	Casting	430±10 Barrer	43±3	[51]
CO ₂ /CH ₄	LDH (CO ₃ ²⁻)	Spin-casting	150 GPU	33	[151]
CO ₂ /N ₂	MgAl-CO ₃ LDH	Vacuum-suction	$2.07 \times 10^{-7} \text{ mol} \cdot \text{m}^{-2} \cdot \text{s}^{-1} \cdot \text{Pa}^{-1}$	35	[149]
CO ₂ /N ₂	MoS ₂ -Pebax/PDMS/PSf	Drop-coating	64 Barrer	93	[185]
CO ₂ /N ₂	MoS ₂ SILM	Vacuum filtration	47.88 GPU	131.42	[186]
CO ₂ /CH ₄				43.52	
CO ₂ /N ₂	WS ₂ SILM	Vacuum filtration	47.3 GPU	153.21	[19]
CO ₂ /CH ₄				68.81	
C ₂ H ₄ /C ₂ H ₆	Ag/IL-GO	Vacuum filtration Spin-coating	72.5 GPU	215	[145]
<i>n</i> -Butane/ <i>i</i> -butane	MFI	Vacuum filtration	1923 GPU	58	[36]

breakthrough in the development of 2D membranes, there are remaining problems for 2D membranes that should be addressed before their practical utilization. 1) The swelling problem of some 2D lamellar membranes, such as MXene and GO membranes is still one of the most important issues, hindering their applications in liquid systems, such as ion sieving. Facile, effective and universal strategy should be proposed to solve this problem, with potential of promoting the development of lamellar membranes. 2) The second one is the facile scale-up technology. The main reason that 2D membranes cannot beat polymeric membranes is the scale-up industrialization of 2D membranes. It is totally different to produce 2D membranes with huge effective membrane area coupled to membrane modules comparing with lab-scale preparation. The nonselective defects within 2D membranes should be avoided during scale-up production. Most 2D membranes are prepared by the traditional method of vacuum-assisted filtration, where several hours are usually needed to assemble a membrane, which is time-consuming. More importantly, it is difficult to prepare defect-free and homogenous 2D membranes with large area by vacuum filtration, because the driving force across the porous substrate (pressure difference) along the radial direction will be different (different, e.g., at the edge and centre position), resulting in inhomogeneous membrane structure and sacrificial separation performance. Therefore, the preparation method of 2D lamellar membranes is a key bottle neck that blocks their scale-up for industrialization and applications. Electrostatic deposition seems to be a good way to produce 2D membranes with large area, which has many advantages such as facile and rapid operation, homogenous stacking structure and low energy cost. Up to now, it is still difficult to prepare 2D membranes with exactly homogeneous microstructure, especially in a large scale of membrane area. Hence, more

simple and cost-effective ways for fabricating 2D membranes need to be studied further. Furthermore, the issues such as the steady production of high-quality nanosheets with high yield, together with how to scale up such atom-thick membranes into applicable separation devices need to be further studied. Besides, development of robust 2D membranes with stable separation performance under realistic operational conditions is also important. 3) Moreover, the mass transport mechanisms in the confined nanochannels/subnanochannels within 2D membranes also need to be discovered via more cases, including the simulation models, diffusion laws that are different from the classical fluid mechanics, the interaction between molecules/ions and wall of nanochannels. The understanding of mass transportation behavior in 2D membranes from the atomic level and theoretical breakthrough of the molecules/ions transport in confined nanochannels/subnanochannels will also help to design novel structures of 2D lamellar membranes or pave new routes for next generation of membranes.

In the next few years, 2D membranes will be focused on the types basing on porous nanosheets, where the prolonged zigzag pathway in traditional lamellar membranes based on non-porous nanosheets can be avoided effectively, while sharply reducing the permeation resistance. In addition, the ultrathin 2D membranes with thickness of only several nanometers will be another research hotspot, where the mass transportation route can be decreased maximumly, resulting in ultrahigh permeance and promoting further applications of 2D membranes.

Nevertheless, 2D membranes are considered to be promising candidates for separation as the next-generation membranes, which have the possibility to surpass the upper bound of separation performance. It is undeniable that there is still a long way to go for the wide practical utilization of 2D membranes.

Table 2 Summary of nanofiltration for 2D-material membranes

Feed system	Membrane	Fabrication approach	Water flux	Rejection/%	Ref.
Evans blue	<i>g</i> -C ₃ N ₄	Vacuum filtration	29 L·m ⁻² ·h ⁻¹ ·bar ⁻¹	87	[26]
Evans blue	<i>g</i> -C ₃ N ₄ -PAA	Vacuum filtration	117 L·m ⁻² ·h ⁻¹ ·bar ⁻¹	83	[69]
Evans blue	MXene	Vacuum filtration	1084 L·m ⁻² ·h ⁻¹ ·bar ⁻¹	90	[16]
Evans blue	MoS ₂	Vacuum filtration	245 L·m ⁻² ·h ⁻¹ ·bar ⁻¹	89	[177]
Evans blue	WS ₂	Vacuum filtration	1850 L·m ⁻² ·h ⁻¹ ·bar ⁻¹	82	[178]
Evans blue	NSC-GO	Vacuum filtration	695 L·m ⁻² ·h ⁻¹ ·bar ⁻¹	83.5	[126]
Evans blue	NbN/GO	Vacuum filtration	20 L·m ⁻² ·h ⁻¹ ·bar ⁻¹	98	[142]
Rhodamine B	CDs-GO	Vacuum filtration	439 L·m ⁻² ·h ⁻¹	96.9	[130]
Rhodamine B	Fe ₃ O ₄ @rGO	Filtration-disposition	296 L·m ⁻² ·h ⁻¹ ·bar ⁻¹	98.14	[128]
Rhodamine B	rGO-TH	Vacuum filtration	8526±30 L·m ⁻² ·h ⁻¹ ·bar ⁻¹	99±1	[121]
Rhodamine B	Tp-AD	Vacuum filtration	596 L·m ⁻² ·h ⁻¹ ·bar ⁻¹	98	[61]
Rhodamine B	SWCNT/GO	Vacuum filtration	710±50 L·m ⁻² ·h ⁻¹ ·bar ⁻¹	97.4±0.3	[132]
Rhodamine B	<i>g</i> -C ₃ N ₄ NT/rGO	Vacuum filtration	4.87 L·m ⁻² ·h ⁻¹ ·bar ⁻¹	98	[134]
Rhodamine B	CA/GO-TiO ₂	Vacuum filtration	33.2 L·m ⁻² ·h ⁻¹	99.4	[131]
Rhodamine B	GO/TiO ₂	Vacuum filtration	89.6 L·m ⁻² ·h ⁻¹ ·bar ⁻¹	99.3	[135]
Rhodamine B	rGO-TiO ₂	Secondary growth	9.82 L·m ⁻² ·h ⁻¹ ·bar ⁻¹	98.5	[136]
Methylene blue	TAMoS ₂	Vacuum filtration	10000 L·m ⁻² ·h ⁻¹ ·bar ⁻¹	98.26	[182]
Methylene blue	BPEI/GO	Vacuum filtration	2.09 L·m ⁻² ·h ⁻¹ ·bar ⁻¹	96.4	[117]
Methylene blue	WS ₂ /GO	Vacuum filtration	159.6 L·m ⁻² ·h ⁻¹ ·bar ⁻¹	96.3	[139]
Methylene blue	GO/MXene	Vacuum filtration	71.9 L·m ⁻² ·h ⁻¹ ·bar ⁻¹	99.5	[141]
Methyl blue	rGO	Vacuum filtration	21.8 L·m ⁻² ·h ⁻¹ ·bar ⁻¹	99.2	[137]
Methyl blue	SPPO/ <i>g</i> -C ₃ N ₄	Vacuum filtration	8867 L·m ⁻² ·h ⁻¹ ·bar ⁻¹	100	[27]
Methyl red	Zn-TCP(Fe)/PEI	Vacuum filtration	4243 L·m ⁻² ·h ⁻¹ ·bar ⁻¹	98.2	[54]
Methyl orange	MgAILDH	Vacuum filtration	298 L·m ⁻² ·h ⁻¹ ·bar ⁻¹	99.5	[161]
Methyl orange	MWNTs/GO	Vacuum filtration	8.69 L·m ⁻² ·h ⁻¹ ·bar ⁻¹	96.1	[133]
Congo red	GO/NH ₂ -Fe ₃ O ₄	Vacuum filtration	15.6 L·m ⁻² ·h ⁻¹ ·bar ⁻¹	94	[129]
Congo red	GO/MoS ₂	Pressure-assisted filtration	~10.2 L·m ⁻² ·h ⁻¹ ·bar ⁻¹	99.6	[138]
Eriochrome black T	MgAl-LDH	<i>In situ</i> growth	566 L·m ⁻² ·h ⁻¹ ·MPa ⁻¹	98.5	[160]
Chrome black T	COF-LZU1	<i>In situ</i> growth	760 L·m ⁻² ·h ⁻¹ ·MPa ⁻¹	98	[64]
Acid yellow 14	<i>c</i> -Ti ₃ C ₂ T _x	Vacuum filtration	344 L·m ⁻² ·h ⁻¹ ·bar ⁻¹	76.4	[167]
NaCl	PHGOM	Dual-flow filtration	1529 L·m ⁻² ·h ⁻¹ ·bar ⁻¹	97	[146]
NaCl	GNM/SWNT	O ₂ plasma drilling	22 L·m ⁻² ·h ⁻¹ ·bar ⁻¹	98.1	[106]
NaCl	MXene	Vacuum filtration	2.8 L·m ⁻² ·h ⁻¹	96.5	[168]
NaCl	MoS ₂	Chemical vapor deposition	> 322 L·m ⁻² ·h ⁻¹ ·bar ⁻¹	> 99	[18]
NaCl	MoS ₂	Vacuum filtration	33.7 L·m ⁻² ·h ⁻¹ ·bar ⁻¹	82	[181]
NaCl	GO-PVAm-Silica	Pressure-assisted filtration	80.2±0.8 kg·m ⁻² ·h ⁻¹	99.99	[123]
NaCl	<i>g</i> -C ₃ N ₄ -PA	Interfacial polymerization	45 g·m ⁻² ·h ⁻¹	98	[76]
MgCl ₂	GO	Pressure-assisted filtration Dip-coating	51.2 L·m ⁻² ·h ⁻¹ ·bar ⁻¹	93.2	[15]
CoCl ₂	Al-MOF	Vacuum filtration	2.22 mol·m ⁻² ·h ⁻¹ ·bar ⁻¹	100	[47]
Na ₂ SO ₄	COFs@CNFs	Vacuum filtration	42.8 L·m ⁻² ·h ⁻¹ ·bar ⁻¹	96.8	[24]

Acknowledgements The authors gratefully acknowledge the funding from the National Natural Science Foundation of China (Grant Nos. 22022805, 22078107 and 51621001) and Guangdong Natural Science Funds for Distinguished Young Scholar (No. 2017A030306002).

References

1. Robeson L M. The upper bound revisited. *Journal of Membrane Science*, 2008, 320(1-2): 390–400
2. Novoselov K S, Geim A K, Morozov S V, Jiang D, Zhang Y, Dubonos S V, Grigorieva I V, Firsov A A. Electric field effect in atomically thin carbon films. *Science*, 2004, 306(5696): 666–669
3. Duong D D. Adsorption Analysis: Equilibria and Kinetics. London: London Imperial College Press, 1998, 239–240
4. Peng Y, Li Y, Ban Y, Jin H, Jiao W, Liu X, Yang W. Metal-organic framework nanosheets as building blocks for molecular sieving membranes. *Science*, 2014, 346(6215): 1356–1359
5. Shen J, Liu G, Huang K, Chu Z, Jin W, Xu N. Subnanometer two-dimensional graphene oxide channels for ultrafast gas sieving. *ACS Nano*, 2016, 10(3): 3398–3409
6. Shen J, Liu G, Ji Y, Liu Q, Cheng L, Guan K, Zhang M, Liu G, Xiong J, Yang J, et al. 2D MXene nanofilms with tunable gas transport channels. *Advanced Functional Materials*, 2018, 28(31): 1801511
7. Wang J, Chen P, Shi B, Guo W, Jaroniec M, Qiao S. A regularly channeled lamellar membrane for unparalleled water and organics permeation. *Angewandte Chemie International Edition*, 2018, 130(23): 6930–6934
8. Ibrahim A, Lin Y S. Gas permeation and separation properties of large-sheet stacked graphene oxide membranes. *Journal of Membrane Science*, 2017, 550: 238–245
9. Nielsen L E. Models for the permeability of filled polymer systems. *Journal of Macromolecular Science: Part A—Chemistry*, 1967, 1(5): 929–942
10. Tan C, Cao X, Wu X J, He Q, Yang J, Zhang X, Chen J, Zhao W, Han S, Nam G H, et al. Recent advances in ultrathin two-dimensional nanomaterials. *Chemical Reviews*, 2017, 117(9): 6225–6331
11. Samori P, Palermo V, Feng X. Chemical approaches to 2D materials. *Advanced Materials*, 2016, 28(29): 6027–6029
12. Zhang H. Ultrathin two-dimensional nanomaterials. *ACS Nano*, 2015, 9(10): 9451–9469
13. Nie L, Goh K, Wang Y, Lee J, Huang Y, Karahan H E, Zhou K, Guiver M D, Bae T H. Realizing small-flake graphene oxide membranes for ultrafast size-dependent organic solvent nanofiltration. *Science Advances*, 2020, 6(17): eaaz9184
14. Li H, Song Z, Zhang X, Huang Y, Li S, Mao Y, Ploehn H J, Bao Y, Yu M. Ultrathin, molecular-sieving graphene oxide membranes for selective hydrogen separation. *Science*, 2013, 342(6154): 95–98
15. Zhang M, Guan K, Ji Y, Liu G, Jin W, Xu N. Controllable ion transport by surface-charged graphene oxide membrane. *Nature Communications*, 2019, 10: 1253
16. Ding L, Wei Y, Wang Y, Chen H, Caro J, Wang H. A two-dimensional lamellar membrane: MXene nanosheet stacks. *Angewandte Chemie International Edition*, 2017, 129(7): 1851–1855
17. Ding L, Wei Y, Li L, Zhang T, Wang H, Xue J, Ding L X, Wang S, Caro J, Gogotsi Y. MXene molecular sieving membranes for highly efficient gas separation. *Nature Communications*, 2018, 9: 155
18. Li H, Ko T J, Lee M, Chung H S, Han S S, Oh K H, Sadmani A, Kang H, Jung Y. Experimental realization of few layer two-dimensional MoS₂ membranes of near atomic thickness for high efficiency water desalination. *Nano Letters*, 2019, 19(8): 5194–5204
19. Chen D, Wang W, Ying W, Guo Y, Meng D, Yan Y, Yan R, Peng X. CO₂-philic WS₂ laminated membranes with a nanoconfined ionic liquid. *Journal of Materials Chemistry. A, Materials for Energy and Sustainability*, 2018, 6(34): 16566–16573
20. Kim D, Jeon M, Stottrup B L, Tsapatsis M. Paraxylene ultra-selective zeolite MFI membranes fabricated from nanosheet monolayers at the air-water interface. *Angewandte Chemie International Edition*, 2018, 130(2): 489–494
21. Cao Z, Zeng S, Xu Z, Arvanitis A, Yang S, Gu X, Dong J. Ultrathin ZSM-5 zeolite nanosheet laminated membrane for high-flux desalination of concentrated brines. *Science Advances*, 2018, 4(11): eaau8634
22. Peng Y, Li Y, Ban Y, Yang W. Two-dimensional metal-organic framework nanosheets for membrane-based gas separation. *Angewandte Chemie International Edition*, 2017, 56(33): 9757–9761
23. Wang X, Chi C, Zhang K, Qian Y, Gupta K M, Kang Z, Jiang J, Zhao D. Reversed thermo-switchable molecular sieving membranes composed of two-dimensional metal-organic nanosheets for gas separation. *Nature Communications*, 2017, 8: 14460
24. Yang H, Yang L, Wang H, Xu Z, Zhao Y, Luo Y, Nasir N, Song Y, Wu H, Pan F, et al. Covalent organic framework membranes through a mixed-dimensional assembly for molecular separations. *Nature Communications*, 2019, 10: 2101
25. Ying Y, Tong M, Ning S, Ravi S K, Peh S B, Tan S C, Pennycook S J, Zhao D. Ultrathin two-dimensional membranes assembled by ionic covalent organic nanosheets with reduced apertures for gas separation. *Journal of the American Chemical Society*, 2020, 142(9): 4472–4480
26. Wang Y, Li L, Wei Y, Xue J, Chen H, Ding L, Caro J, Wang H. Water transport with ultralow friction through partially exfoliated g-C₃N₄ nanosheet membranes with self-supporting spacers. *Angewandte Chemie International Edition*, 2017, 56(31): 8974–8980
27. Ran J, Pan T, Wu Y, Chu C, Cui P, Zhang P, Ai X, Fu C F, Yang Z, Xu T. Endowing g-C₃N₄ membranes with superior permeability and stability by using acid spacers. *Angewandte Chemie International Edition*, 2019, 58(46): 16463–16468
28. Tsapatsis M. 2-Dimensional zeolites. *AIChE Journal. American Institute of Chemical Engineers*, 2014, 60(7): 2374–2381
29. Choi M, Na K, Kim J, Sakamoto Y, Ryoo R. Stable single-unit-cell nanosheets of zeolite MFI as active and long-lived catalysts. *Nature*, 2009, 461(7261): 246–249
30. Na K, Choi M, Park W, Sakamoto Y, Terasaki O, Ryoo R. Pillared MFI zeolite nanosheets of a single-unit-cell thickness. *Journal of the American Chemical Society*, 2010, 132(12): 4169–4177

31. Varoon K, Zhang X, Elyassi B, Brewer D D, Gettel M, Kumar S, Lee J A, Maheshwari S, Mittal A, Sung C Y, et al. Dispersible exfoliated zeolite nanosheets and their application as a selective membrane. *Science*, 2011, 334(6052): 72–75
32. Agrawal K V, Topuz B, Jiang Z, Nguenkam K, Elyassi B, Francis L F, Tsapatsis M. Solution-processable exfoliated zeolite nanosheets purified by density gradient centrifugation. *AIChE Journal*. American Institute of Chemical Engineers, 2013, 59(9): 3458–3467
33. Pham T C, Nguyen T H, Yoon K B. Gel-free secondary growth of uniformly oriented silica MFI zeolite films and application for xylene separation. *Angewandte Chemie*, 2013, 125(33): 8855–8860
34. Agrawal K V, Topuz B, Pham T, Thanh T, Sauer N, Rangnekar N, Zhang H, Narasimharao K, Basahel S N, Francis L F, et al. Oriented MFI membranes by gel-less secondary growth of sub-100 nm MFI-nanosheet seed layers. *Advanced Materials*, 2015, 27(21): 3243–3249
35. Jeon M Y, Kim D, Kumar P, Lee P S, Rangnekar N, Bai P, Shete M, Elyassi B, Lee H S, Narasimharao K, et al. Ultra-selective high-flux membranes from directly synthesized zeolite nanosheets. *Nature*, 2017, 543(7647): 690–694
36. Min B, Yang S, Korde A, Kwon Y H, Jones C W, Nair S. Continuous zeolite MFI membranes fabricated from 2D MFI nanosheets on ceramic hollow fibers. *Angewandte Chemie*, 2019, 131(24): 8285–8289
37. Choi J, Lai Z, Ghosh S, Beving D E, Yan Y, Tsapatsis M. Layer-by-layer deposition of barrier and permselective *c*-oriented-MCM-22 silica composite films. *Industrial & Engineering Chemistry Research*, 2007, 46(22): 7096–7106
38. Choi J, Tsapatsis M. MCM-22 silica selective flake nanocomposite membranes for hydrogen separations. *Journal of the American Chemical Society*, 2010, 132(2): 448–449
39. Choi S, Coronas J, Jordan E, Oh W, Nair S, Onorato F, Shantz D F, Tsapatsis M. Layered silicates by swelling of AMH-3 and nanocomposite membranes. *Angewandte Chemie International Edition*, 2008, 47(3): 552–555
40. Kim W, Lee J S, Bucknall D G, Koros W J, Nair S. Nanoporous layered silicate AMH-3/cellulose acetate nanocomposite membranes for gas separations. *Journal of Membrane Science*, 2013, 441: 129–136
41. Galve A, Sieffert D, Vispe E, Téllez C, Coronas J, Staudt C. Copolyimide mixed matrix membranes with oriented microporous titanosilicate JDF-L1 sheet particles. *Journal of Membrane Science*, 2011, 370(1-2): 131–140
42. Castarlenas S, Gorgojo P, Casado C, Masheshwari S, Tsapatsis M, Téllez C, Coronas J. Melt compounding of swollen titanosilicate JDF-L1 with polysulfone to obtain mixed matrix membranes for H₂/CH₄ separation. *Industrial & Engineering Chemistry Research*, 2013, 52(5): 1901–1907
43. Galve A, Sieffert D, Staudt C, Ferrando M, Güell C, Téllez C, Coronas J. Combination of ordered mesoporous silica MCM-41 and layered titanosilicate JDF-L1 fillers for 6FDA-based copolyimide mixed matrix membranes. *Journal of Membrane Science*, 2013, 431: 163–170
44. Wei X L, Pan W Y, Li X, Pan M, Huo C F, Yang R, Chao Z S. MCM-22 zeolite-induced synthesis of thin sodalite zeolite membranes. *Chemistry of Materials*, 2020, 32(1): 333–340
45. Ma N, Wei J, Liao R, Tang C Y. Zeolite-polyamide thin film nanocomposite membranes: towards enhanced performance for forward osmosis. *Journal of Membrane Science*, 2012, 405-406: 149–157
46. Peng Y, Yang W. 2D metal-organic framework materials for membrane-based separation. *Advanced Materials Interfaces*, 2020, 7(1): 1901514
47. Jian M, Qiu R, Xia Y, Lu J, Chen Y, Gu Q, Liu R, Hu C, Qu J, Wang H, et al. Ultrathin water-stable metal-organic framework membranes for ion separation. *Science Advances*, 2020, 6(23): eaay3998
48. Rodenas T, Luz I, Prieto G, Seoane B, Miro H, Corma A, Kapteijn F, Llabres I X F X, Gascon J. Metal-organic framework nanosheets in polymer composite materials for gas separation. *Nature Materials*, 2015, 14(1): 48–55
49. Kang Z, Peng Y, Hu Z, Qian Y, Chi C, Yeo L Y, Tee L, Zhao D. Mixed matrix membranes composed of two-dimensional metal-organic framework nanosheets for pre-combustion CO₂ capture: a relationship study of filler morphology versus membrane performance. *Journal of Materials Chemistry. A, Materials for Energy and Sustainability*, 2015, 3(41): 20801–20810
50. Cheng Y, Wang X, Jia C, Wang Y, Zhai L, Wang Q, Zhao D. Ultrathin mixed matrix membranes containing two-dimensional metal-organic framework nanosheets for efficient CO₂/CH₄ separation. *Journal of Membrane Science*, 2017, 539: 213–223
51. Yang Y, Goh K, Wang R, Bae T H. High-performance nanocomposite membranes realized by efficient molecular sieving with CuBDC nanosheets. *Chemical Communications*, 2017, 53(30): 4254–4257
52. Yang F, Wu M, Wang Y, Ashtiani S, Jiang H. A GO-induced assembly strategy to repair MOF nanosheet-based membrane for efficient H₂/CO₂ separation. *ACS Applied Materials & Interfaces*, 2019, 11(1): 990–997
53. Zhong Z, Yao J, Chen R, Low Z, He M, Liu J Z, Wang H. Oriented two-dimensional zeolitic imidazolate framework-L membranes and their gas permeation properties. *Journal of Materials Chemistry. A, Materials for Energy and Sustainability*, 2015, 3(30): 15715–15722
54. Ang H, Hong L. Polycationic polymer-regulated assembling of 2D MOF nanosheets for high-performance nanofiltration. *ACS Applied Materials & Interfaces*, 2017, 9(33): 28079–28088
55. Li Y, Liu H, Wang H, Qiu J, Zhang X. GO-guided direct growth of highly oriented metal-organic framework nanosheet membranes for H₂/CO₂ separation. *Chemical Science (Cambridge)*, 2018, 9(17): 4132–4141
56. Li Y, Lin L, Tu M, Nian P, Howarth A J, Farha O K, Qiu J, Zhang X. Growth of ZnO self-converted 2D nanosheet zeolitic imidazolate framework membranes by an ammonia-assisted strategy. *Nano Research*, 2018, 11(4): 1850–1860
57. Nian P, Liu H, Zhang X. Bottom-up fabrication of two-dimensional Co-based zeolitic imidazolate framework tubular membranes consisting of nanosheets by vapor phase transformation of Co-based gel for H₂/CO₂ separation. *Journal of Membrane Science*, 2019, 573: 200–209

58. Lin L C, Choi J, Grossman J C. Two-dimensional covalent triazine framework as an ultrathin-film nanoporous membrane for desalination. *Chemical Communications*, 2015, 51(80): 14921–14924
59. Tong M, Yang Q, Ma Q, Liu D, Zhong C. Few-layered ultrathin covalent organic framework membranes for gas separation: a computational study. *Journal of Materials Chemistry. A, Materials for Energy and Sustainability*, 2016, 4(1): 124–131
60. Wang Y, Li J, Yang Q, Zhong C. Two-dimensional covalent triazine framework membrane for helium separation and hydrogen purification. *ACS Applied Materials & Interfaces*, 2016, 8(13): 8694–8701
61. Yao J, Liu C, Liu X, Guo J, Zhang S, Zheng J, Li S. Azobenzene-assisted exfoliation of 2D covalent organic frameworks into large-area, few-layer nanosheets for high flux and selective molecular separation membrane. *Journal of Membrane Science*, 2020, 601: 117864
62. Dey K, Pal M, Rout K C, Kunjattu H S, Das A, Mukherjee R, Kharul U K, Banerjee R. Selective molecular separation by interfacially crystallized covalent organic framework thin films. *Journal of the American Chemical Society*, 2017, 139(37): 13083–13091
63. Matsumoto M, Valentino L, Stiehl G M, Balch H B, Corcos A R, Wang F, Ralph D C, Mariñas B J, Dichtel W R. Lewis-acid-catalyzed interfacial polymerization of covalent organic framework films. *Chem*, 2018, 4(2): 308–317
64. Fan H, Gu J, Meng H, Knebel A, Caro J. High-flux membranes based on the covalent organic framework COF-LZU1 for selective dye separation by nanofiltration. *Angewandte Chemie International Edition*, 2018, 57(15): 4083–4087
65. Fan H, Mundstock A, Feldhoff A, Knebel A, Gu J, Meng H, Caro J. Covalent organic framework-covalent organic framework bilayer membranes for highly selective gas separation. *Journal of the American Chemical Society*, 2018, 140(32): 10094–10098
66. Li Y, Wu Q, Guo X, Zhang M, Chen B, Wei G, Li X, Li X, Li S, Ma L. Laminated self-standing covalent organic framework membrane with uniformly distributed subnanopores for ionic and molecular sieving. *Nature Communications*, 2020, 11: 599
67. Li F, Qu Y, Zhao M. Efficient helium separation of graphitic carbon nitride membrane. *Carbon*, 2015, 95: 51–57
68. Liu Y, Xie D, Song M, Jiang L, Fu G, Liu L, Li J. Water desalination across multilayer graphitic carbon nitride membrane: insights from non-equilibrium molecular dynamics simulations. *Carbon*, 2018, 140: 131–138
69. Wang Y, Liu L, Xue J, Hou J, Ding L, Wang H. Enhanced water flux through graphitic carbon nitride nanosheets membrane by incorporating polyacrylic acid. *AIChE Journal. American Institute of Chemical Engineers*, 2018, 64(6): 2181–2188
70. Wang Y, Wu N, Wang Y, Ma H, Zhang J, Xu L, Albolqany M K, Liu B. Graphite phase carbon nitride based membrane for selective permeation. *Nature Communications*, 2019, 10: 2500
71. Cao K, Jiang Z, Zhang X, Zhang Y, Zhao J, Xing R, Yang S, Gao C, Pan F. Highly water-selective hybrid membrane by incorporating $g\text{-C}_3\text{N}_4$ nanosheets into polymer matrix. *Journal of Membrane Science*, 2015, 490: 72–83
72. Wang Y, Ou R, Wang H, Xu T. Graphene oxide modified graphitic carbon nitride as a modifier for thin film composite forward osmosis membrane. *Journal of Membrane Science*, 2015, 475: 281–289
73. Chen J, Li Z, Wang C, Wu H, Liu G. Synthesis and characterization of $g\text{-C}_3\text{N}_4$ nanosheet modified polyamide nanofiltration membranes with good permeation and antifouling properties. *RSC Advances*, 2016, 6(113): 112148–112157
74. Tian Z, Wang S, Wang Y, Ma X, Cao K, Peng D, Wu X, Wu H, Jiang Z. Enhanced gas separation performance of mixed matrix membranes from graphitic carbon nitride nanosheets and polymers of intrinsic microporosity. *Journal of Membrane Science*, 2016, 514: 15–24
75. Zhao H, Chen S, Quan X, Yu H, Zhao H. Integration of microfiltration and visible-light-driven photocatalysis on $g\text{-C}_3\text{N}_4$ nanosheet/reduced graphene oxide membrane for enhanced water treatment. *Applied Catalysis B: Environmental*, 2016, 194: 134–140
76. Gao X, Li Y, Yang X, Shang Y, Wang Y, Gao B, Wang Z. Highly permeable and antifouling reverse osmosis membranes with acidified graphitic carbon nitride nanosheets as nanofillers. *Journal of Materials Chemistry. A, Materials for Energy and Sustainability*, 2017, 5(37): 19875–19883
77. Wang J, Li M, Zhou S, Xue A, Zhang Y, Zhao Y, Zhong J, Zhang Q. Graphitic carbon nitride nanosheets embedded in poly(vinyl alcohol) nanocomposite membranes for ethanol dehydration via pervaporation. *Separation and Purification Technology*, 2017, 188: 24–37
78. Bunch J S, Verbridge S S, Alden J S, Zande A M, Parpia J M, Craighead H G, McEuen P L. Impermeable atomic membranes from graphene sheets. *Nano Letters*, 2008, 8: 2458–2462
79. Cohen Tanugi D, Grossman J C. Water desalination across nanoporous graphene. *Nano Letters*, 2012, 12(7): 3602–3608
80. Sint K, Wang B, Král P. Selective ion passage through functionalized graphene nanopores. *Journal of the American Chemical Society*, 2008, 130(49): 16448–16449
81. Jiang D, Cooper V R, Dai S. Porous graphene as the ultimate membrane for gas separation. *Nano Letters*, 2009, 9: 4019–4024
82. Hauser A W, Schwerdtfeger P. Methane-selective nanoporous graphene membranes for gas purification. *Physical Chemistry Chemical Physics*, 2012, 14(38): 13292–13298
83. Sun C, Boutilier M S, Au H, Poesio P, Bai B, Karnik R, Hadjiconstantinou N G. Mechanisms of molecular permeation through nanoporous graphene membranes. *Langmuir*, 2014, 30(2): 675–682
84. Shan M, Xue Q, Jing N, Ling C, Zhang T, Yan Z, Zheng J. Influence of chemical functionalization on the CO_2/N_2 separation performance of porous graphene membranes. *Nanoscale*, 2012, 4(17): 5477–5482
85. Liu H, Chen Z, Dai S, Jiang D. Selectivity trend of gas separation through nanoporous graphene. *Journal of Solid State Chemistry*, 2015, 224: 2–6
86. Nouri M, Ghasemzadeh K, Iulianelli A. Theoretical evaluation of graphene membrane performance for hydrogen separation using molecular dynamic simulation. *Membranes*, 2019, 9(9): 110
87. Yuan Z, Misra R P, Rajan A G, Strano M S, Blankschtein D. Analytical prediction of gas permeation through graphene

- nanopores of varying sizes: understanding transitions across multiple transport regimes. *ACS Nano*, 2019, 13(10): 11809–11824
88. Xu Y, Xu J, Yang C. Separation of diverse alkenes from C₂–C₄ alkanes through nanoporous graphene membranes via local size sieving. *Journal of Membrane Science*, 2019, 584: 227–235
89. Garaj S, Hubbard W, Reina A, Kong J, Branton D, Golovchenko J A. Graphene as a subnanometre trans-electrode membrane. *Nature*, 2010, 467(7312): 190–193
90. Fischbein M D, Drndić M. Electron beam nanosculpting of suspended graphene sheets. *Applied Physics Letters*, 2008, 93(11): 113107
91. Celebi K, Buchheim J, Wyss R M, Droudian A, Gasser P, Shorubalko I, Kye J, Lee C, Park H G. Ultimate permeation across atomically thin porous graphene. *Science*, 2014, 344(6181): 289–292
92. Fan Z, Zhao Q, Li T, Yan J, Ren Y, Feng J, Wei T. Easy synthesis of porous graphene nanosheets and their use in supercapacitors. *Carbon*, 2012, 50(4): 1699–1703
93. O'Hem S C, Boutilier M S, Idrobo J C, Song Y, Kong J, Laoui T, Atieh M, Karnik R. Selective ionic transport through tunable subnanometer pores in single-layer graphene membranes. *Nano Letters*, 2014, 14(3): 1234–1241
94. Koenig S P, Wang L, Pellegrino J, Bunch J S. Selective molecular sieving through porous graphene. *Nature Nanotechnology*, 2012, 7(11): 728–732
95. Surwade S P, Smirnov S N, Vlassiouk I V, Unocic R R, Veith G M, Dai S, Mahurin S M. Water desalination using nanoporous single-layer graphene. *Nature Nanotechnology*, 2015, 10(5): 459–464
96. Sun C, Wen B, Bai B. Recent advances in nanoporous graphene membrane for gas separation and water purification. *Science Bulletin*, 2015, 60(21): 1807–1823
97. Liu G, Jin W, Xu N. Two-dimensional-material membranes: a new family of high-performance separation membranes. *Angewandte Chemie International Edition*, 2016, 55(43): 13384–13397
98. Li G, Li Y, Liu H, Guo Y, Li Y, Zhu D. Architecture of graphdiyne nanoscale films. *Chemical Communications*, 2010, 46(19): 3256–3258
99. Blankenburg S, Bieri M, Fasel R, Mullen K, Pignedoli C A, Passerone D. Porous graphene as an atmospheric nanofilter. *Small*, 2010, 6(20): 2266–2271
100. Kidambi P R, Nguyen G D, Zhang S, Chen Q, Kong J, Warner J, Li A P, Karnik R. Facile fabrication of large-area atomically thin membranes by direct synthesis of graphene with nanoscale porosity. *Advanced Materials*, 2018, 30(49): 1804977
101. Huang S, Dakhchoune M, Luo W, Oveisi E, He G, Rezaei M, Zhao J, Alexander D T L, Zuttel A, Strano M S, et al. Single-layer graphene membranes by crack-free transfer for gas mixture separation. *Nature Communications*, 2018, 9: 2632
102. Wang S, Dai S, Jiang D. Continuously tunable pore size for gas separation via a bilayer nanoporous graphene membrane. *ACS Applied Nano Materials*, 2018, 2(1): 379–384
103. Zhao J, He G, Huang S, Villalobos L F, Dakhchoune M, Bassas H, Agrawal K V. Etching gas-sieving nanopores in single-layer graphene with an angstrom precision for high-performance gas mixture separation. *Science Advances*, 2019, 5(1): eaav1851
104. Sun C, Zhu S, Liu M, Shen S, Bai B. Selective molecular sieving through a large graphene nanopore with surface charges. *Journal of Physical Chemistry Letters*, 2019, 10(22): 7188–7194
105. Choi K, Droudian A, Wyss R M, Schlichting K P, Park H G. Multifunctional wafer-scale graphene membranes for fast ultra-filtration and high permeation gas separation. *Science Advances*, 2018, 4(11): eaau0476
106. Yang Y, Yang X, Liang L, Gao Y, Cheng H, Li X, Zou M, Ma R, Yuan Q, Duan X. Large-area graphene-nanomesh/carbon-nanotube hybrid membranes for ionic and molecular nanofiltration. *Science*, 2019, 364(6445): 1057–1062
107. Lin L C, Grossman J C. Atomistic understandings of reduced graphene oxide as an ultrathin-film nanoporous membrane for separations. *Nature Communications*, 2015, 6: 8335
108. Wang P, Li W, Du C, Zheng X, Sun X, Yan Y, Zhang J. CO₂/N₂ separation via multilayer nanoslit graphene oxide membranes: molecular dynamics simulation study. *Computational Materials Science*, 2017, 140: 284–289
109. Zheng H, Zhu L, He D, Guo T, Li X, Chang X, Xue Q. Two-dimensional graphene oxide membrane for H₂/CH₄ separation: insights from molecular dynamics simulations. *International Journal of Hydrogen Energy*, 2017, 42(52): 30653–30660
110. Li W, Zhang L, Zhang X, Zhang M, Liu T, Chen S. Atomic insight into water and ion transport in 2D interlayer nanochannels of graphene oxide membranes: implication for desalination. *Journal of Membrane Science*, 2020, 596: 117744
111. Nair R R, Wu H A, Jayaram P N, Grigorieva I V, Geim A K. Unimpeded permeation of water through helium-leak-tight graphene-based membranes. *Science*, 2012, 335(6067): 442–444
112. Chen L, Shi G, Shen J, Peng B, Zhang B, Wang Y, Bian F, Wang J, Li D, Qian Z, et al. Ion sieving in graphene oxide membranes via cationic control of interlayer spacing. *Nature*, 2017, 550(7676): 380–383
113. Yeh C N, Raidongia K, Shao J, Yang Q H, Huang J. On the origin of the stability of graphene oxide membranes in water. *Nature Chemistry*, 2014, 7(2): 166–170
114. Long Y, Wang K, Xiang G, Song K, Zhou G, Wang X. Molecule channels directed by cation-decorated graphene oxide nanosheets and their application as membrane reactors. *Advanced Materials*, 2017, 29(16): 1606093
115. Chen L, Huang L, Zhu J. Stitching graphene oxide sheets into a membrane at a liquid/liquid interface. *Chemical Communications*, 2014, 50(100): 15944–15947
116. Liu J, Wang N, Yu L J, Karton A, Li W, Zhang W, Guo F, Hou L, Cheng Q, Jiang L, et al. Bioinspired graphene membrane with temperature tunable channels for water gating and molecular separation. *Nature Communications*, 2017, 8: 2011
117. Nam Y T, Choi J, Kang K M, Kim D W, Jung H T. Enhanced stability of laminated graphene oxide membranes for nanofiltration via interstitial amide bonding. *ACS Applied Materials & Interfaces*, 2016, 8(40): 27376–27382
118. Hu M, Mi B. Enabling graphene oxide nanosheets as water separation membranes. *Environmental Science & Technology*, 2013, 47(8): 3715–3723
119. Hung W S, Tsou C H, De Guzman M, An Q F, Liu Y L, Zhang Y M, Hu C C, Lee K R, Lai J Y. Cross-linking with diamine

- monomers to prepare composite graphene oxide-framework membranes with varying *d*-spacing. *Chemistry of Materials*, 2014, 26(9): 2983–2990
120. Jia Z, Wang Y. Covalently crosslinked graphene oxide membranes by esterification reactions for ions separation. *Journal of Materials Chemistry. A, Materials for Energy and Sustainability*, 2015, 3(8): 4405–4412
121. Thebo K H, Qian X, Zhang Q, Chen L, Cheng H M, Ren W. Highly stable graphene-oxide-based membranes with superior permeability. *Nature Communications*, 2018, 9: 1486
122. Liang F, Liu Q, Zhao J, Guan K, Mao Y, Liu G, Gu X, Jin W. Ultrafast water-selective permeation through graphene oxide membrane with water transport promoters. *AIChE Journal. American Institute of Chemical Engineers*, 2020, 66(2): e16812
123. Pan F, Li Y, Song Y, Wang M, Zhang Y, Yang H, Wang H, Jiang Z. Graphene oxide membranes with fixed interlayer distance via dual crosslinkers for efficient liquid molecular separations. *Journal of Membrane Science*, 2020, 595: 117486
124. Huang L, Li Y, Zhou Q, Yuan W, Shi G. Graphene oxide membranes with tunable semipermeability in organic solvents. *Advanced Materials*, 2015, 27(25): 3797–3802
125. Huang L, Chen J, Gao T, Zhang M, Li Y, Dai L, Qu L, Shi G. Reduced graphene oxide membranes for ultrafast organic solvent nanofiltration. *Advanced Materials*, 2016, 28(39): 8669–8674
126. Huang H, Song Z, Wei N, Shi L, Mao Y, Ying Y, Sun L, Xu Z, Peng X. Ultrafast viscous water flow through nanostrand-channelled graphene oxide membranes. *Nature Communications*, 2013, 4: 2979
127. Wang S, Mahalingam D, Sutisna B, Nunes S P. 2D-dual-spacing channel membranes for high performance organic solvent nanofiltration. *Journal of Materials Chemistry. A, Materials for Energy and Sustainability*, 2019, 7(19): 11673–11682
128. Zhang M, Guan K, Shen J, Liu G, Fan Y, Jin W. Nanoparticles@rGO membrane enabling highly enhanced water permeability and structural stability with preserved selectivity. *AIChE Journal. American Institute of Chemical Engineers*, 2017, 63(11): 5054–5063
129. Dong L, Li M, Zhang S, Si X, Bai Y, Zhang C. NH₂-Fe₃O₄-regulated graphene oxide membranes with well-defined laminar nanochannels for desalination of dye solutions. *Desalination*, 2020, 476: 114227
130. Wang W, Eftekhari E, Zhu G, Zhang X, Yan Z, Li Q. Graphene oxide membranes with tunable permeability due to embedded carbon dots. *Chemical Communications*, 2014, 50(86): 13089–13092
131. Liu Y, Yu Z, Peng Y, Shao L, Li X, Zeng H. A novel photocatalytic self-cleaning TiO₂ nanorods inserted graphene oxide-based nanofiltration membrane. *Chemical Physics Letters*, 2020, 749: 137424
132. Gao S J, Qin H, Liu P, Jin J. SWCNT-intercalated GO ultrathin films for ultrafast separation of molecules. *Journal of Materials Chemistry. A, Materials for Energy and Sustainability*, 2015, 3(12): 6649–6654
133. Han Y, Jiang Y, Gao C. High-flux graphene oxide nanofiltration membrane intercalated by carbon nanotubes. *ACS Applied Materials & Interfaces*, 2015, 7(15): 8147–8155
134. Wei Y, Zhu Y, Jiang Y. Photocatalytic self-cleaning carbon nitride nanotube intercalated reduced graphene oxide membranes for enhanced water purification. *Chemical Engineering Journal*, 2019, 356: 915–925
135. Han R, Wu P. High-performance graphene oxide nanofiltration membrane with continuous nanochannels prepared by the *in situ* oxidation of MXene. *Journal of Materials Chemistry. A, Materials for Energy and Sustainability*, 2019, 7(11): 6475–6481
136. Yu J, Zhang Y, Chen J, Cui L, Jing W. Solvothermal-induced assembly of 2D-2D rGO-TiO₂ nanocomposite for the construction of nanochannel membrane. *Journal of Membrane Science*, 2020, 600: 117870
137. Han Y, Xu Z, Gao C. Ultrathin graphene nanofiltration membrane for water purification. *Advanced Functional Materials*, 2013, 23(29): 3693–3700
138. Zhang P, Gong J L, Zeng G M, Song B, Cao W, Liu H Y, Huan S Y, Peng P. Novel “loose” GO/MoS₂ composites membranes with enhanced permeability for effective salts and dyes rejection at low pressure. *Journal of Membrane Science*, 2019, 574: 112–123
139. Cheng P, Chen Y, Gu Y H, Yan X, Lang W Z. Hybrid 2D WS₂/GO nanofiltration membranes for finely molecular sieving. *Journal of Membrane Science*, 2019, 591: 117308
140. Wei S, Xie Y, Xing Y, Wang L, Ye H, Xiong X, Wang S, Han K. Two-dimensional graphene oxide/MXene composite lamellar membranes for efficient solvent permeation and molecular separation. *Journal of Membrane Science*, 2019, 582: 414–422
141. Liu T, Liu X, Graham N, Yu W, Sun K. Two-dimensional MXene incorporated graphene oxide composite membrane with enhanced water purification performance. *Journal of Membrane Science*, 2020, 593: 117431
142. Kunimatsu M, Nakagawa K, Yoshioka T, Shintani T, Yasui T, Kamio E, Tsang S C E, Li J, Matsuyama H. Design of niobate nanosheet-graphene oxide composite nanofiltration membranes with improved permeability. *Journal of Membrane Science*, 2020, 595: 117598
143. Morelos Gomez A, Cruz Silva R, Muramatsu H, Ortiz Medina J, Araki T, Fukuyo T, Tejima S, Takeuchi K, Hayashi T, Terrones M, et al. Effective NaCl and dye rejection of hybrid graphene oxide/graphene layered membranes. *Nature Nanotechnology*, 2017, 12(11): 1083–1088
144. Kim H W, Yoon H W, Yoon S M, Yoo B M, Ahn B K, Cho Y H, Shin H J, Yang H, Paik U, Kwon S, et al. Selective gas transport through few-layered graphene and graphene oxide membranes. *Science*, 2013, 342(6154): 91–95
145. Dou H, Xu M, Jiang B, Wen G, Zhao L, Wang B, Yu A, Bai Z, Sun Y, Zhang L, et al. Bioinspired graphene oxide membranes with dual transport mechanisms for precise molecular separation. *Advanced Functional Materials*, 2019, 29(50): 1905229
146. Wen Q, Jia P, Cao L, Li J, Quan D, Wang L, Zhang Y, Lu D, Jiang L, Guo W. Electric-field-induced ionic sieving at planar graphene oxide heterojunctions for miniaturized water desalination. *Advanced Materials*, 2020, 32(16): 1903954
147. Wang Q, O’Hare D. Recent advances in the synthesis and application of layered double hydroxide (LDH) nanosheets. *Chemical Reviews*, 2012, 112(7): 4124–4155
148. Kim T W, Sahimi M, Tsotsis T T. Preparation of hydrotalcite thin

- films using an electrophoretic technique. *Industrial & Engineering Chemistry Research*, 2008, 47: 9127–9132
149. Kim T W, Sahimi M, Tsotsis T T. The preparation and characterization of hydrotalcite thin films. *Industrial & Engineering Chemistry Research*, 2009, 48: 5794–5801
150. Liu Y, Wang N, Cao Z, Caro J. Molecular sieving through interlayer galleries. *Journal of Materials Chemistry. A, Materials for Energy and Sustainability*, 2014, 2(5): 1235–1238
151. Liu Y, Wu H, Min L, Song S, Yang L, Ren Y, Wu Y, Zhao R, Wang H, Jiang Z. 2D layered double hydroxide membranes with intrinsic breathing effect toward CO₂ for efficient carbon capture. *Journal of Membrane Science*, 2020, 598: 117663
152. Liu Y, Wang N, Diestel L, Steinbach F, Caro J. MOF membrane synthesis in the confined space of a vertically aligned LDH network. *Chemical Communications*, 2014, 50(32): 4225–4227
153. Liu Y, Wang N, Pan J H, Steinbach F, Caro J. *In situ* synthesis of MOF membranes on ZnAl-CO₃ LDH buffer layer-modified substrates. *Journal of the American Chemical Society*, 2014, 136(41): 14353–14356
154. Liu Y, Peng Y, Wang N, Li Y, Pan J H, Yang W, Caro J. Significantly enhanced separation using ZIF-8 membranes by partial conversion of calcined layered double hydroxide precursors. *ChemSusChem*, 2015, 8(21): 3582–3586
155. Fan H, Peng M, Strauss I, Mundstock A, Meng H, Caro J. High-flux vertically aligned 2D covalent organic framework membrane with enhanced hydrogen separation. *Journal of the American Chemical Society*, 2020, 142(15): 6872–6877
156. Lu P, Liang S, Qiu L, Gao Y, Wang Q. Thin film nanocomposite forward osmosis membranes based on layered double hydroxide nanoparticles blended substrates. *Journal of Membrane Science*, 2016, 504: 196–205
157. Lu P, Liang S, Zhou T, Mei X, Zhang Y, Zhang C, Umar A, Wang Q. Layered double hydroxide/graphene oxide hybrid incorporated polysulfone substrate for thin-film nanocomposite forward osmosis membranes. *RSC Advances*, 2016, 6(61): 56599–56609
158. Zhao Y, Li N, Yuan F, Zhang H, Xia S. Preparation and characterization of hydrophilic and antifouling poly(ether sulfone) ultrafiltration membranes modified with Zn-Al layered double hydroxides. *Journal of Applied Polymer Science*, 2016, 133(39): 43988–43998
159. Arefi Oskoui S, Khataee A, Vatanpour V. Effect of solvent type on the physicochemical properties and performance of NLDH/PVDF nanocomposite ultrafiltration membranes. *Separation and Purification Technology*, 2017, 184: 97–118
160. Wang N, Huang Z, Li X, Li J, Ji S, An Q F. Tuning molecular sieving channels of layered double hydroxides membrane with direct intercalation of amino acids. *Journal of Materials Chemistry. A, Materials for Energy and Sustainability*, 2018, 6(35): 17148–17155
161. Ang E H, Velioglu S, Chew J W. Tunable affinity separation enables ultrafast solvent permeation through layered double hydroxide membranes. *Journal of Membrane Science*, 2019, 591: 117318
162. Naguib M, Kurtoglu M, Presser V, Lu J, Niu J, Heon M, Hultman L, Gogotsi Y, Barsoum M W. Two-dimensional nanocrystals produced by exfoliation of Ti₃AlC₂. *Advanced Materials*, 2011, 23(37): 4248–4253
163. Naguib M, Mochalin V N, Barsoum M W, Gogotsi Y. 25th anniversary article: MXenes: a new family of two-dimensional materials. *Advanced Materials*, 2014, 26(7): 992–1005
164. Ren C E, Hatzell K B, Alhabet M, Ling Z, Mahmoud K A, Gogotsi Y. Charge- and size-selective ion sieving through Ti₃C₂T_x MXene membranes. *Journal of Physical Chemistry Letters*, 2015, 6(20): 4026–4031
165. Li L, Zhang T, Duan Y, Wei Y, Dong C, Ding L, Qiao Z, Wang H. Selective gas diffusion in two-dimensional MXene lamellar membranes: insights from molecular dynamics simulations. *Journal of Materials Chemistry. A, Materials for Energy and Sustainability*, 2018, 6(25): 11734–11742
166. Wu X, Cui X, Wu W, Wang J, Li Y, Jiang Z. Elucidating ultrafast molecular permeation through well-defined 2D nanochannels of lamellar membranes. *Angewandte Chemie International Edition*, 2019, 58(51): 18524–18529
167. Xing Y, Akonkwa G, Liu Z, Ye H, Han K. Crumpled two-dimensional Ti₃C₂T_x MXene lamellar membranes for solvent permeation and separation. *ACS Applied Nano Materials*, 2020, 3(2): 1526–1534
168. Ding L, Li L, Liu Y, Wu Y, Lu Z, Deng J, Wei Y, Caro J, Wang H. Effective ion sieving with Ti₃C₂T_x MXene membranes for production of drinking water from seawater. *Nature Sustainability*, 2020, 3: 296–302
169. Lu Z, Wei Y, Deng J, Ding L, Li Z K, Wang H. Self-crosslinked MXene (Ti₃C₂T_x) membranes with good antishrinkage property for monovalent metal ion exclusion. *ACS Nano*, 2019, 13(9): 10535–10544
170. Wu X, Hao L, Zhang J, Zhang X, Wang J, Liu J. Polymer-Ti₃C₂T_x composite membranes to overcome the trade-off in solvent resistant nanofiltration for alcohol-based system. *Journal of Membrane Science*, 2016, 515: 175–188
171. Hao L, Zhang H, Wu X, Zhang J, Wang J, Li Y. Novel thin-film nanocomposite membranes filled with multi-functional Ti₃C₂T_x nanosheets for task-specific solvent transport. *Composites. Part A, Applied Science and Manufacturing*, 2017, 100: 139–149
172. Shamsabadi A A, Isfahani A P, Salestan S K, Rahimpour A, Ghalei B, Sivaniah E, Soroush M. Pushing rubbery polymer membranes to be economic for CO₂ separation: embedment with Ti₃C₂T_x MXene Nanosheets. *ACS Applied Materials & Interfaces*, 2020, 12(3): 3984–3992
173. Gao L, Li C, Huang W, Mei S, Lin H, Ou Q, Zhang Y, Guo J, Zhang F, Xu S, et al. MXene/polymer membranes: synthesis, properties, and emerging applications. *Chemistry of Materials*, 2020, 32(5): 1703–1747
174. Heiranian M, Farimani A B, Aluru N R. Water desalination with a single-layer MoS₂ nanopore. *Nature Communications*, 2015, 6: 8616
175. Kou J, Yao J, Wu L, Zhou X, Lu H, Wu F, Fan J. Nanoporous two-dimensional MoS₂ membranes for fast saline solution purification. *Physical Chemistry Chemical Physics*, 2016, 18(32): 22210–22216
176. Li W, Yang Y, Weber J K, Zhang G, Zhou R. Tunable, strain-controlled nanoporous MoS₂ filter for water desalination. *ACS Nano*, 2016, 10(2): 1829–1835

177. Sun L, Huang H, Peng X. Laminar MoS₂ membranes for molecule separation. *Chemical Communications*, 2013, 49(91): 10718–10720
178. Sun L, Ying Y, Huang H, Song Z, Mao Y, Xu Z, Peng X. Ultrafast molecule separation through layered WS₂ nanosheet membranes. *ACS Nano*, 2014, 8(6): 6304–6311
179. Hirunpinyopas W, Prestat E, Worrall S D, Haigh S J, Dryfe R A W, Bissett M A. Desalination and nanofiltration through functionalized laminar MoS₂ Membranes. *ACS Nano*, 2017, 11(11): 11082–11090
180. Ang E H, Chew J W. Two-dimensional transition-metal dichalcogenide-based membrane for ultrafast solvent permeation. *Chemistry of Materials*, 2019, 31(24): 10002–10007
181. Ries L, Petit E, Michel T, Diogo C C, Gervais C, Salameh C, Bechelany M, Balme S, Miele P, Onofrio N, et al. Enhanced sieving from exfoliated MoS₂ membranes via covalent functionalization. *Nature Materials*, 2019, 18(10): 1112–1117
182. Hu W, Cui X, Xiang L, Gong L, Zhang L, Gao M, Wang W, Zhang J, Liu F, Yan B, et al. Tannic acid modified MoS₂ nanosheet membranes with superior water flux and ion/dye rejection. *Journal of Colloid and Interface Science*, 2020, 560: 177–185
183. Wang D, Wang Z, Wang L, Hu L, Jin J. Ultrathin membranes of single-layered MoS₂ nanosheets for high-permeance hydrogen separation. *Nanoscale*, 2015, 7(42): 17649–17652
184. Achari A, Sahana S, Eswaramoorthy M. High performance MoS₂ membranes: effects of thermally driven phase transition on CO₂ separation efficiency. *Energy & Environmental Science*, 2016, 9(4): 1224–1228
185. Shen Y, Wang H, Zhang X, Zhang Y. MoS₂ nanosheets functionalized composite mixed matrix membrane for enhanced CO₂ capture via surface drop-coating method. *ACS Applied Materials & Interfaces*, 2016, 8(35): 23371–23378
186. Chen D, Ying W, Guo Y, Ying Y, Peng X. Enhanced gas separation through nanoconfined ionic liquid in laminated MoS₂ membrane. *ACS Applied Materials & Interfaces*, 2017, 9(50): 44251–44257